

ARTICLE

Specific loading of oncolytic VSV on CAR enhances CAR-T cell signaling and antitumor activity

Fan Xing^{1,2}, Xuemei Wang³, Zeying Li¹, Liangying Zheng¹, Zuda Huang², Jieqing Guo¹, Zhihui Xi¹, Huolun Feng⁴, Baijin Xia¹, Yingtong Lin³, Fei Yu¹, Jie Chen⁵, and Hui Zhang³

Oncolytic viruses (OVs) have been shown to increase the efficacy of chimeric antigen receptor (CAR) T cells in treating solid tumors. However, their combined effect has been limited by the unbalanced distribution of two agents in tumor tissue and viral infection-mediated CAR-T cell exhaustion. Here, we designed a CAR moiety by inserting the CR2 and CR3 domains (CR2/3-CAR) of low-density lipoprotein receptor, which is the viral receptor of oncolytic vesicular stomatitis virus (VSV) mutant (VSVA51), enabling specific loading of VSVA51 onto CAR-T cells. The anchored VSVA51 could be released from CAR-T cells and efficiently delivered to tumor tissue. Further investigation revealed that the cross-connection between viral envelope proteins and CR2/3-CAR moieties facilitated forming antigen-free CAR clusters and antigen-induced CAR synapse, triggered CAR signaling transduction, and directly pre-activated the CAR-T cells. Consequently, this approach potently enhanced the proliferation, metabolic fitness, and immunological activities of CAR-T cells, and subsequently enhanced the OV/CAR-T synergetic cytotoxicity, revealing an effective strategy for treating solid tumors.

Introduction

Adoptively transferred T cells engineered to express chimeric antigen receptors (CARs) have shown success in eliminating hematopoietic tumors and some autoimmune diseases (Albelda, 2024; Wang et al., 2024). However, their efficacy against solid tumors has been limited so far. Combining oncolytic viruses (OVs) are being actively explored to overcome the resistance to CAR-T cells in solid tumors (Chen et al., 2024; Evgin et al., 2020; Evgin et al., 2022; Park et al., 2020; Wang et al., 2023; Zheng et al., 2022), which include OV delivery of therapeutic transgenes such as cytokines (Nishio et al., 2014; Watanabe et al., 2018), anti-checkpoint antibodies (Abs) (Rosewell Shaw et al., 2017; Tanoue et al., 2017), or the CAR antigen itself to the tumor (Park et al., 2020) to potentiate CAR-T cell efficacy. Local intratumoral injection of OVs may enhance CAR-T cell trafficking into the virus-injected tumors, reshape local immunosuppression, and improve CAR-T cell effector function (Ajina and Maher, 2017; Chen et al., 2024). However, a key issue is how to formulate and optimize the combination of two agents. Delivering OVs and CAR-T cells separately or in a physically mixed form in vivo causes the distribution of two agents in different populations of tumor cells, thereby reducing the combined benefit (Zheng et al., 2022). Although the combination of CAR-T

cells with OVs via spin-infection procedure could increase the infection of OV on CAR-T cells, this nonspecific loading leads to cell exhaustion or proliferation inhibition of CAR-T through the activation of IFN signaling pathway (Evgin et al., 2020; Zheng et al., 2022).

Glioblastoma (GBM) is a malignant primary brain tumor in adults that is highly immunosuppressive and intractably resistant to therapy (Jackson et al., 2019; Schaff and Mellinghoff, 2023). GBM patients have a median survival of only 15 mo (Dewdney et al., 2023; van den Bent et al., 2023). Vesicular stomatitis virus (VSV) and its mutant VSVΔ51 were introduced as a potent oncolytic candidate that replicates effectively in gliomas (Chen et al., 2023; Stojdl et al., 2003; Xiao et al., 2022; Xing et al., 2021). The low-density lipoprotein receptor (LDLR) is a major entry receptor for VSV to enter host cells, and viral envelope protein VSV-G can bind independently to two distinct CR domains (CR2 and CR3) of LDLR (Finkelshtein et al., 2013; Nikolic et al., 2018).

To meet the requirement of increasing OV/CAR-T synergetic effect, we attempted to design a two-in-one combination strategy via loading OVs onto the CAR-T cells. Specifically, we add the component of VSV Δ 51 receptor into the extracellular part of CAR

¹Medical Research Institute, Guangdong Provincial People's Hospital (Guangdong Academy of Medical Sciences), Southern Medical University, Guangzhou, China; ²School of Pharmaceutical Sciences, Southern Medical University, Guangzhou, China; ³Department of Pathogen Biology and Biosecurity, Key Laboratory of Tropical Disease Control of Ministry of Education, Institute of Human Virology, Zhongshan School of Medicine, Sun Yat-sen University, Guangzhou, China; ⁴Department of Gastrointestinal Surgery Department of General Surgery Guangdong Provincial People's Hospital (Guangdong Academy of Medical Sciences), Southern Medical University, Guangzhou, China; ⁵Department of Medical Oncology, The Third Affiliated Hospital, Sun Yat-sen University, Guangzhou, China.

Correspondence to Hui Zhang: zhangh92@mail.sysu.edu.cn; Jie Chen: chjie23@mail.sysu.edu.cn.

© 2025 Xing et al. This article is distributed under the terms as described at https://rupress.org/pages/terms102024/.





moiety to increase the specific loading amount of VSVΔ51 onto CAR-T cells. We found that this strategy not only increase the surface-loading of oncolytic VSVΔ51 on CAR-T cells but also significantly enhanced functional activities of CAR-T cells. Further mechanical studies indicated that the cross-interaction between viral envelope protein VSV-G and CAR moiety harboring CR2 and CR3 domain significantly triggered the CAR signal transduction and induced more efficient immunological synapse (IS) formation to pre-activate the CAR-T cells.

Results

Specific loading of OV VSVΔ51 onto CAR-T cells with chimeric viral receptor domains CR2 and CR3 (CR2/3–CAR-T^{VSV})

To increase loading amount of OVs onto CAR-T cells, we explored adding the components of the viral receptor of OVs into the CAR moiety (Fig. 1 A). We modified the CAR structures by inserting the CR2 and CR3 domains derived from oncolytic VSVΔ51 viral receptor into the anti-epidermal growth factor receptor (EGFR)-specific CAR (EGFR-CAR) moiety at different sites (Fig. 1 B). These different CAR moieties were named (1) CAR-CR2, (2) CAR-CR3, (3) CR2-CAR, (4) CR3-CAR, and (5) CR2-CR3-CAR (CR2/3-CAR), respectively. Different CAR moieties were equally expressed on the cell surface of CAR-T (Fig. S1 A). These CAR-T cells were co-incubated with VSVΔ51 (multiplicity of infection [MOI] = 10) on ice for virus loading. Among different groups, the EGFR-CAR-T cells exhibited a lower ability to load the VSVΔ51, while CR2/3-EGFR-CAR-T cells exhibited the highest ratio of VSV-G-positive cells (Fig. 1 C) and highest level of genomic viral RNA VSV-G and VSV-N (Fig. 1 D) after VSV Δ 51 loading.

Because of the advantage of CR2/3-CAR for virus loading, we focused on this design for further functional evaluations of the B7 homolog 3 protein (B7H3)-specific CAR-T and the IL-13 receptor subunit alpha 2 (IL13Ra2)-specific CAR-T cells. We did not find any significant expression difference between CAR and CR2/3-CAR moiety on B7H3-CAR-T (Fig. S1 B) and IL13Rα2-CAR-T cells (Fig. S1 C). We observed an approximately fivefold higher ratio of VSV-G-positive cells in CR2/3-CAR-T cells compared to conventional CAR-T cells in both B7H3- and IL13Rα2-CAR-T models (Fig. 1, E and F). In the B7H3-CAR-T model, fluorescence microscope analysis confirmed that CR2/3-CAR-T cells loaded with VSVΔ51 (CR2/3-CAR-TVSV) showed higher level of viral protein VSV-G on the surface of CAR-T cells with some aggregation, compared with the CAR-T cells loaded with VSV Δ 51 (CAR-T^{VSV}; Fig. 1 G). Further, the scanning electron microscope also indicated that the attachment of viral particles on the surface of CR2/3-CAR-T cells was significantly increased (Fig. 1 H). It is notable that the insertion of CR2/3 domain into CAR moieties slightly decreases the CAR-T cell-mediated cytotoxicity of target tumor cells at high ratios of effector cells to target cells (Fig. S1, D-F). These results confirmed that CR2/3-CAR moiety significantly enhances loading efficiency of oncolytic VSVΔ51, while only slightly reduces the tumor-killing capacity of CAR-T cells.

Considering that viral infection of OVs can stimulate type I IFN response and lead to functional exhaustion of CAR-T cells

(Evgin et al., 2020), we examined the internalization of surface VSV Δ 51 and type I IFN response of CAR-T cells. Compared with CAR-T^{VSV}, CR2/3-CAR-T^{VSV} showed a lower rate of virus entry into cells (Fig. 1, I and J) and the lower expression level of IFNB1, ISG15, and CXCL10 (Fig. 1 K). The co-expression of the inhibitory receptors PD-1, TIM-3, and LAG-3 on CAR-T^{VSV} cells were significantly upregulated, while the exhaustion markers were significantly reduced in CR2/3-CAR-T^{VSV} compared with CAR-T^{VSV} (Fig. 1 L). These findings suggest that the specific loading on CR2/3-CAR reduced the internalization of VSV Δ 51 and relieved the viral infection-mediated exhaustion of CAR-T cells.

CR2/3-CAR-T cells efficiently delivered VSV Δ 51 to GBM cells in vitro and in vivo

It is important to examine whether the anchored VSV Δ 51 could be effectively released from the CR2/3–CAR-T cell surface when CAR contacts tumor-specific antigens on tumor cells, we labeled VSV Δ 51 with cyanine 7 (CY7) and found that the mean fluorescence intensity of the CY7-labeled VSV Δ 51 was significantly decreased after incubating with the target U87 glioma cells (Fig. 2 A), indicating that the release of VSV Δ 51 from C2/3–CAR-T cells was triggered by competitive interaction between tumor antigen and CAR-T or by membrane fusion between the viral receptor on tumor cells and VSV Δ 51.

To further determine whether CR2/3-CAR-T can function as an efficient virus carrier and systemically deliver VSV Δ 51 to tumor sites, we engineered the recombinant VSVΔ51 to express luciferase (VSV-luc) for measuring virus distribution in vivo and in vitro (Fig. 2 B). The in vitro coculture assay of glioma cells and the CAR-T cells loaded with VSV-luc viruses (CAR-T $^{\rm VSV-luc}$) revealed that CR2/3-CAR-TVSV-luc group showed higher luciferase activity compared with CAR-TVSV-luc group in B7H3-CAR-T and IL13Rα2-CAR-T models, respectively (Fig. 2 C and Fig. S1 G). We next measured the viral delivery in vivo using B7H3-CAR-T model and i.v. injected VSV-luc, CAR-TVSV-luc, or CR2/3-CAR-T^{VSV-luc} into NCG mice bearing U87 xenograft (Fig. 2 D). Bioluminescence imaging analysis revealed that i.v. injection of VSV-luc delivered limited amount of viruses into intracranial tumor (Fig. 2, E and F). The CR2/3-CAR-TVSV-luc efficiently delivered VSV-luc into intracranial tumors and significantly improved the viral delivery at early time point and prolonged the stay time of VSV-luc up to 3 days (Fig. 2, E and F). However, we could not detect the remarkable bioluminescence signal of VSV-luc after 7 days of injection, indicating that most of VSV-luc were eliminated at late time point. Immunofluorescence analyses of mouse brain sections demonstrated that injection of CR2/3-CAR-TVSV-luc promoted the virus perfusion within tumor, compared with VSV-luc and CAR-TVSV-luc group (Fig. 2 G). Analysis of the genomic viral RNA of VSV-G showed that CR2/3-CAR- $T^{VSV-luc}$ significantly increase the VSV Δ 51 replication in intracranial tumors at both 3 and 7 days (Fig. 2 H). For the EGFR-CAR-T model, we also confirmed that CR2/3-CAR-TVSV-luc also efficiently delivered VSV-luc into intracranial tumors (Fig. S1, H and I). The above data indicated that the anchored VSV Δ 51 on the CR2/3-CAR-T could be released and efficiently delivered into intracranial tumor tissue.



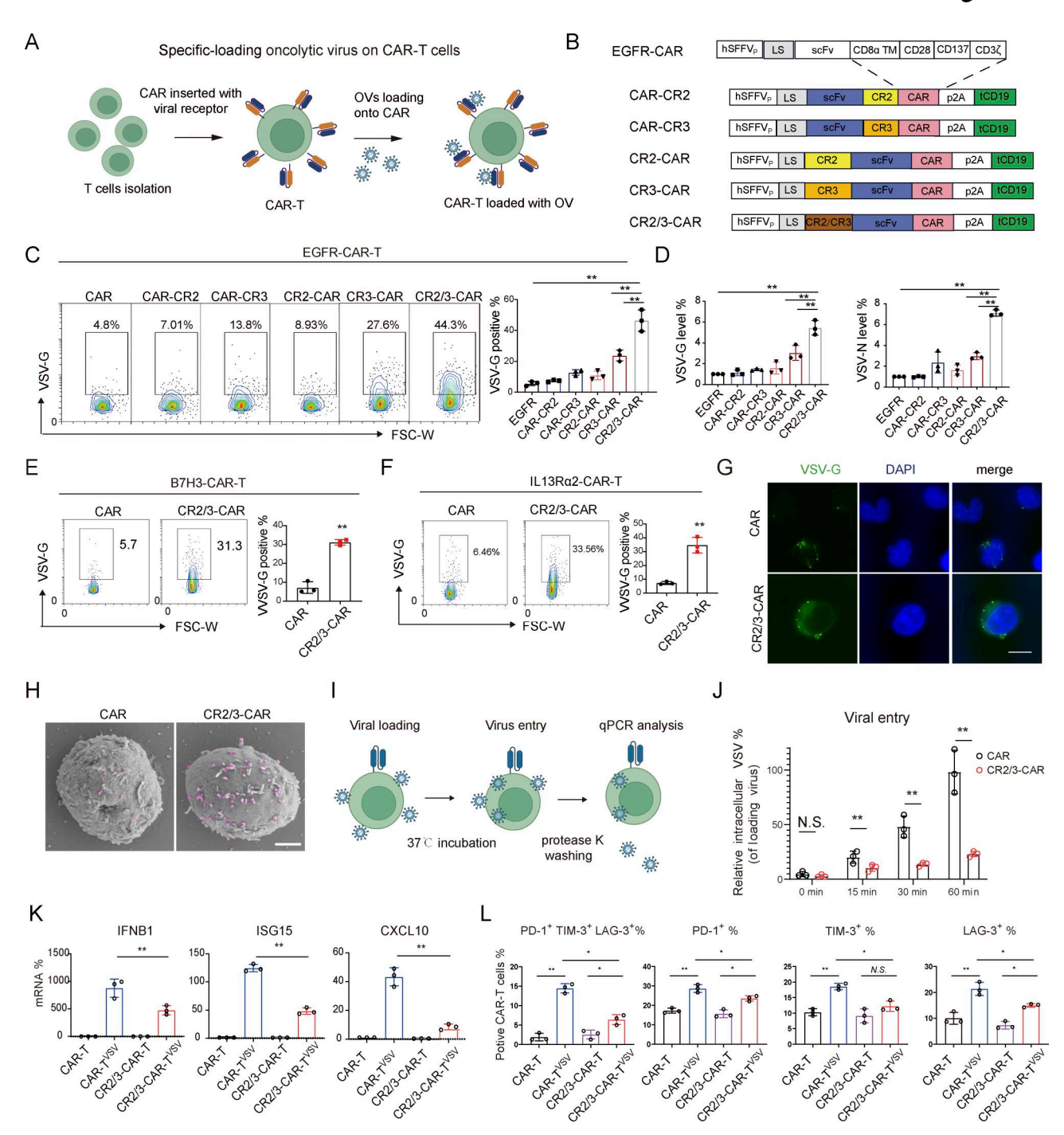


Figure 1. **CR2/3 domain derived from viral receptor enabled the surface loading of oncolytic VSVΔ51 onto CAR-T cells. (A)** Illustration of modified CAR structure for increasing specific loading of OVs on the cell surface of CAR-T cells. **(B)** Illustration for different strategies of EGFR-CAR structure: (1) CAR-CR2, (2) CAR-CR3, (3) CR2-CAR, (4) CR3-CAR, and (5) CR2-CAR3-CAR (CR2/3-CAR). **(C)** Flow cytometry analysis for viral loading efficiency by measuring the viral capsid protein VSV-G onto EGFR-CAR-T model (*n* = 3 biological replicates). **(D)** Viral genes *VSV-G* and *VSV-N* were measured by qPCR in EGFR-CAR-T cells (*n* = 3). **(E and F)** Flow cytometry analysis for viral loading efficiency by measuring VSV-G expression onto the B7H3-CAR-T (E) and IL13Rα2-CAR-T (F). The left panel is the representative graph of flow cytometry analysis; the right panel is the quantitative analysis of the ratio of VSV-G-positive cells in CAR-T cells (*n* = 3 biological replicates). **(G)** Immunofluorescence analysis for viral loading efficiency by measuring the VSV-G expression in B7H3-CAR-T cells. Scale bar, 5 μm. **(H)** Scanning electron microscopy images of B7H3-CAR-T cells and CR2/3-B7H3-CAR-T cells loaded with VSVΔ51. Scale bar, 2 μm. **(I)** Illustration for analyzing the rate of viral entry. After preloading VSVΔ51 at 4°C, CAR-T cells were incubated at 37°C for the indicated time from 0 to 60 min and then were washed by protease K to clear the surface virus. **(J)** The rate of viral entry was calculated as the ratio of intracellular VSV-G expression to the total VSV-G expression before protease K washing. The expression of viral gene *VSV-G* was measured by qRT-PCR (*n* = 3 biological replicates). **(K)** The mRNA level of IFNB1, ISG15, and CXCL10 by qRT-PCR measurement. CAR-T cells were preloaded with VSVΔ51 (MOI = 10) or not for 8 h (*n* = 3 biological replicates). **(L)** Flow cytometry analysis for cell exhaustion of CAR-T cells by measuring the expression of Tim-3 and PD-1 *in vitro* (*n* = 3 biological replicates). **(C)**



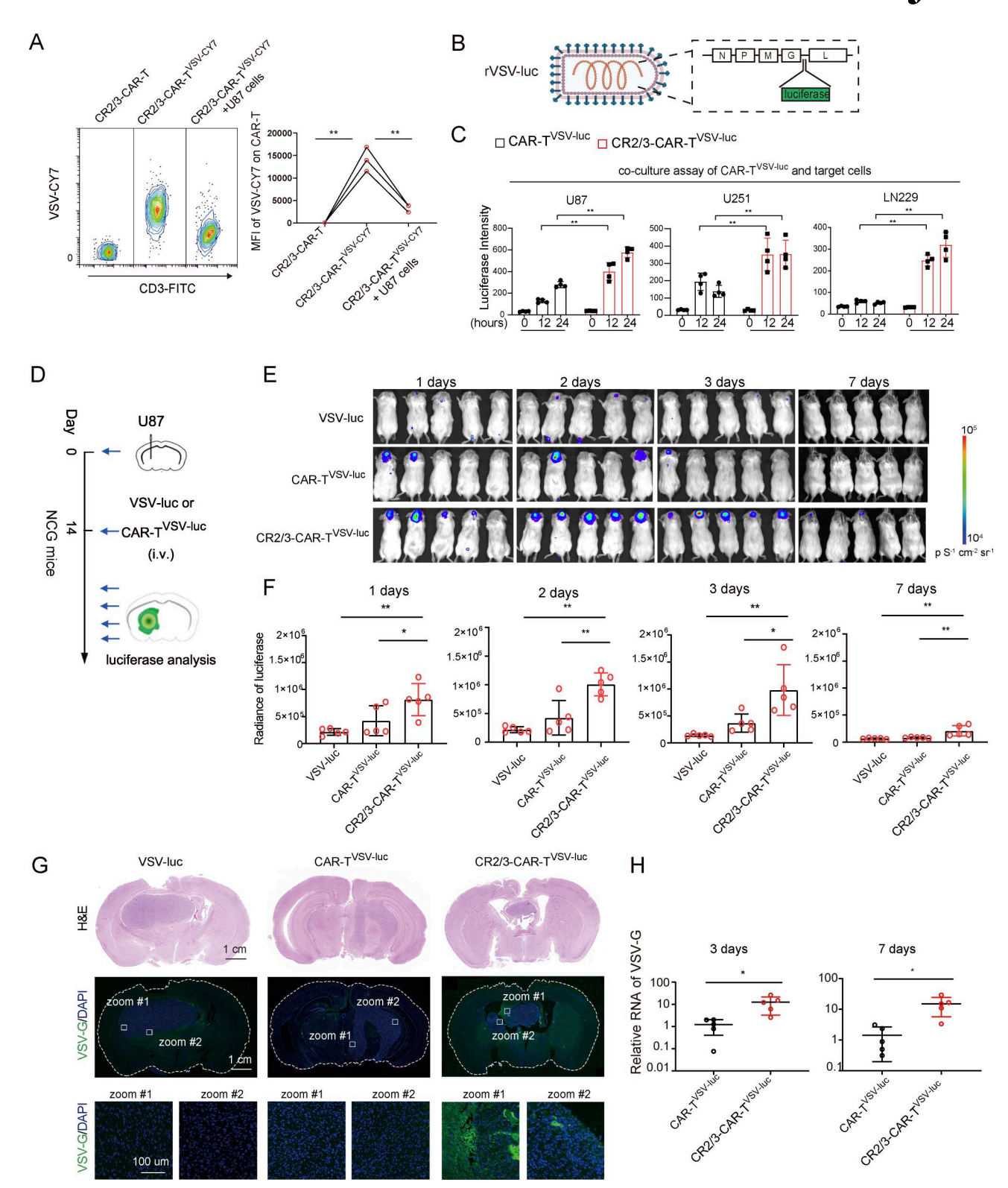


Figure 2. **CR2/3–CAR-T cells efficiently delivered VSVΔ51 to GBM cells** *in vitro* **and** *in vivo*. **(A)** Representative cytometry plots and MFI analysis of VSVΔ51 release from CR2/3–B7H3–CAR-T cells after incubating with U87 cells for 30 min; VSVΔ51 was stained using CY7. **(B)** Generation of recombinant VSVΔ51 to express luciferase (VSV-luc) for measuring the distribution *in vivo* and replication of virus *in vitro*. **(C)** Luciferase activity was measured in LN229, U87, and U251 cells, when cocultured with the B7H3–CAR-T or CR2/3–B7H3–CAR-T cells preloading with the VSV-luc (*n* = 4 biological replicates). **(D–F)** *In vivo* evaluation for viral delivery of B7H3–CAR-T model. **(D)** Diagram depicting monitoring of the *in vivo* virus distribution via bioluminescence imaging of luciferase in U87 xenograft mice. CAR-T or VSV was i.v. injected. **(E)** The bioluminescence imaging of luciferase in U87 xenograft mice at indicated time points from two independent experiments. Two independent experiments were conducted to assess viral signals at indicated time points. **(F)** Quantitative radiance of mice was analyzed (*n* = 5 mice). **(G)** H&E staining and immunofluorescence analysis of U87 intracranial xenograft. The mouse brain tissue sections for H&E staining and



immunofluorescence were consecutive sections. H&E staining revealed the site of brain tumor, while immunofluorescence staining showed the distribution of the viral protein VSV-G. (H) mRNA level of VSV-G in U87 intracranial xenograft was measured (n = 5 mice). Data represent the mean \pm SD from three independent experiments (A), four independent experiments (C), and one representative from two independent experiments (E and H). Statistics by one-way ANOVA with Tukey's post hoc test (A and F) and unpaired two-tailed Student's t test (C and H). *, P < 0.01; N.S., no significance.

Specific loading of VSV particles enhanced the cytotoxicity of CAR-T cells against antigen-positive tumor cells

We next examine the influence of VSV Δ 51 loading on the killing function of CAR-T cells. In the 3D tumor spheroid coculture assay of primary glioma stem cell (GSC-1) and CAR-T cells, we found that CR2/3-CAR-T^{VSV} induced superior cytotoxicity, compared with CAR-T^{VSV} (Fig. 3, A and B). Interestingly, CR2/3-CAR-T ^{VSV} showed a rapid and higher release of effector cytokines such as IFN γ , granzyme B, and TNF α only after 2-4 h since coculture (Fig. 3 C), indicating that VSV loading could enhance the killing function of CR2/3-CAR-T cells before the oncolysis occurred. Given that the above data showed that VSV Δ 51 aggregated on the cell surface of CR2/3-CAR-T cells (Fig. 1 G), we suspected that the specific interaction between VSV Δ 51 and CR2/3-CAR moiety is capable of activating CAR-T cells directly.

To test this hypothesis, we first examined whether the specific interaction between VSV-G protein on viral particle and the CR2/3 fragment in extracellular CAR moiety is required for the above phenomenon. We replaced the VSV-G protein on viral particle by spike protein of SARS-CoV-2 by using the VSV pseudotyped virus packaging system (Fig. 3 D). The VSV-G gene is deleted in the genomic backbone of the VSV (VSV Δ G), and the VSV-G protein (VSVΔG*G) or S protein from SARS-CoV-2 $(VSV\Delta G^*S)$ is incorporated as the membrane protein on the surface of the VSV pseudotyped virus, which is expressed from another plasmid in trans (Nie et al., 2020). Neither $VSV\Delta G^*G$ nor $VSV\Delta G^*S$ recombinant viruses were able to replicate in the CAR-T and tumor cells, which also exclude the oncolysis effect of VSV for cytotoxicity measurement. We found that VSVΔG*G rather than $VSV\Delta G^*S$ loading significantly improved the cytotoxicity effect of CR2/3-CAR-T cells to GSC-1, U87, and LN299 cells (Fig. 3, E-G). Moreover, CR2/3-CAR-T^{VSVΔG*G} did not show enhanced cytotoxicity to antigen KO U87 cells (U87-B7H3-KO; Fig. 3, H and I). There, data suggested that only specific cross-connection between VSV-G proteins on the viral particles and CR2/3 domains on the extracellular CAR moiety pre-activated the CR2/3-CAR-T and enhanced tumor-killing effect of CAR-T cells.

Specific loading of VSVΔ51 directly triggered the CAR signaling transduction and pre-activated the CR2/3-CAR-T cells

Given that VSV loading could directly activate the CR2/3-CAR-T cells before the oncolysis occurred, we next tested the effect of VSV Δ 51 loading on the transcriptional profile of CAR-T cells at antigen-free condition. T cell activation signaling pathways, including "regulation of cytosolic calcium ion concentration," "NF- κ B signaling," and "T cell receptor signaling pathway," were enriched in the CR2/3-CAR-T^{VSV}, compared with CAR-T^{VSV} (Fig. 4, A and B). We confirmed that VSV Δ 51 loading on CR2/3-CAR significantly increased the expression of granzyme B, IFN γ , TNF α , and CD107a of CAR-T at antigen-free condition (Fig. 4, C and D). Further, specific loading of VSV Δ 51 on CR2/3-CAR also

activated the CAR signaling cascade, increasing the phosphorylation of ZAP70, LAT, and PLC γ (Smith-Garvin et al., 2009; Sun et al., 2020) (Fig. 4 E). The calcium flux measurement revealed that VSV Δ 51 loading on CR2/3-CAR induced a significant calcium burst and relatively higher and sustained levels of calcium influx (Fig. 4 F).

We further asked whether the preincubation of CAR antigen could induce the same effect induced by specific loading of virus particles. However, the incubation of soluble B7H3 protein did not promote the functional activity, CAR signaling, and calcium flux in CAR-T cells (Fig. S2, A-D). Furthermore, the preincubation of soluble B7H3 protein also did not enhance the cytotoxicity of B7H3-CAR-T and CR2/3-B7H3-CAR-T cells (Fig. S2, E-G). All the above data suggested that only the complete viral particle, but not dispersing CAR antigen protein, could act as a CAR enhancer.

As the early TCR signaling can induce rapid aerobic glycolysis that enables the acute T cell effector function (Menk et al., 2018), we further examined the metabolic state of CAR-T cells and found that specific loading VSVΔ51 on CR2/3-CAR could elevate both extracellular acidification rate (ECAR) and oxygen consumption rate (OCR) in CR2/3-CAR-T cells (Fig. 4, G and H). We then confirmed by flow cytometry that specific loading VSVΔ51 on CR2/3-CAR enhanced cellular glucose uptake by promoting the entry of 2-NBDG, a fluorescent derivative of glucose (Fig. 4 I). Consistent with the glucose uptake data, analysis of MitoTracker Deep Red staining validated that specific loading VSVΔ51 on CR2/3-CAR also increased mitochondrial mass of CAR-T cells (Fig. 4 J). The proliferation of CR2/3-CAR-T cells was also increased after the specific loading of $VSV\Delta51$ (Fig. 4 K). These data suggested that specific loading VSVΔ51 on CR2/3-CAR triggered CAR signal transduction and promoted T cell polyfunctionality, metabolic fitness, and cell proliferation of CAR-T cells.

Loading of VSV viruses induced CAR clustering and synapse formation on CR2/3-CAR-T cells

Next, we sought to determine the underlying mechanism for VSV loading to pre-activate CR2/3-CAR-T cells. Using super-resolution imaging, we found that CR2/3-B7H3-CAR moiety were significantly clustered than those of B7H3-CAR moiety in the case of VSV Δ 51 loading (Fig. 5 A). Alternatively, we further co-transfected T cells with mcherry-CR2/3-CAR and GFP-CR2/3-CAR and found that specific loading of VSV Δ 51 promoted the co-localization of mcherry-CR2/3-CAR and GFP-CR2/3-CAR (Fig. 5 B), indicating the formation of CAR clustering at antigen-free conditions.

It has been reported that the CAR:antigen complexes can form functional IS in CAR-T cells, although they do not consist of bona fide central, peripheral, or distal supramolecular activation complexes in contrast to canonical TCR to MHC (TCR:MHC) synapse (Chockley et al., 2023; Davenport et al., 2018).



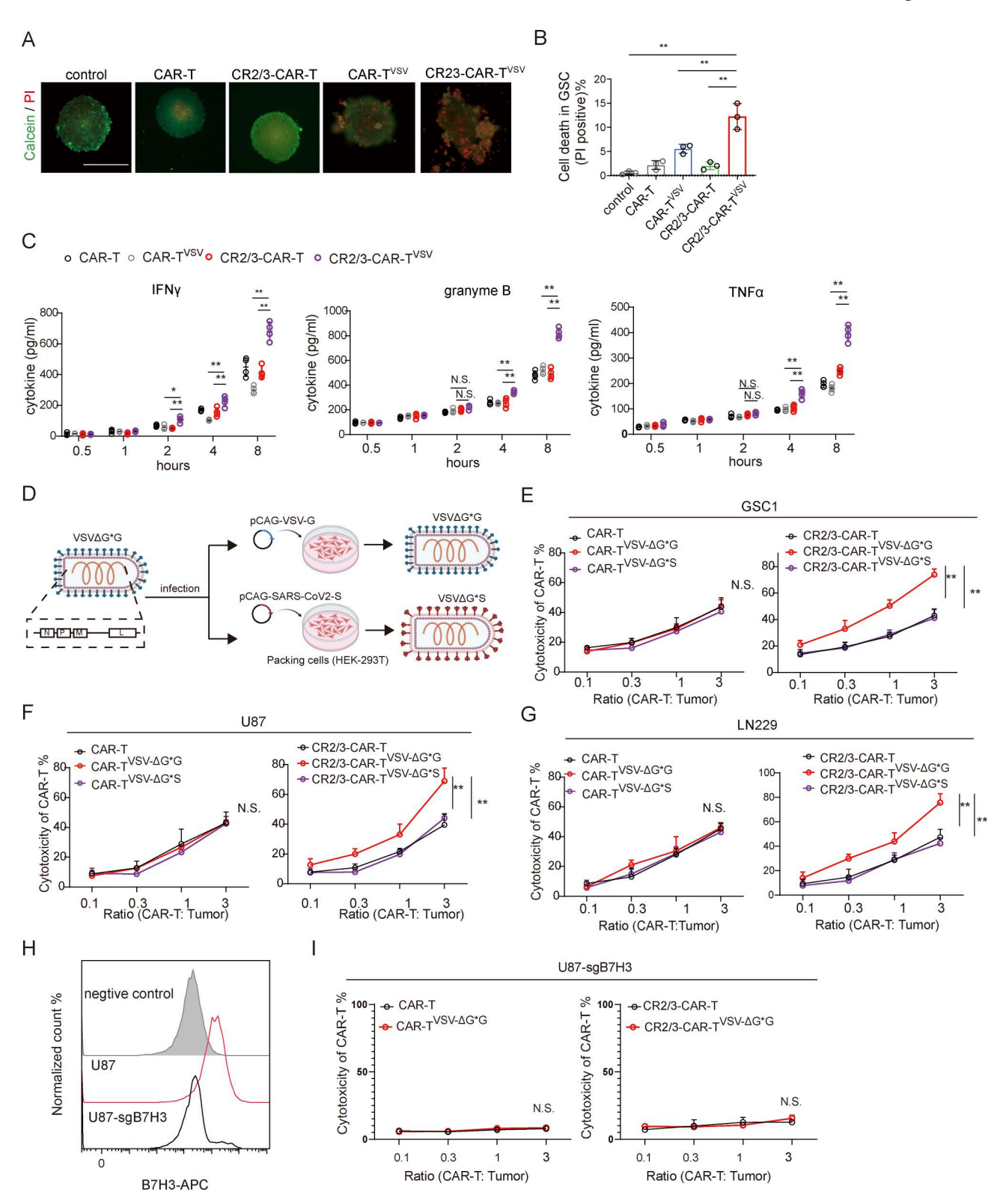


Figure 3. Loading of VSV virus particles enhanced the specific cytotoxicity against CAR antigen-positive tumor cells. (A–C) Coculture experiments of GSC-1 tumor spheroids and CAR-T cells. (A) Cytotoxic effect of CR2/3–B7H3–CAR-T^{VSV} against 3D spheroids of GSC-1 cells was measured by Calcein/PI staining. Representative images are shown. Scale bar, 100 μ m. (B) PI-positive cells was quantified via flow cytometer analysis (n = 3 biological replicates). (C) Quantitative analysis of cytokines IFNY, granzyme B, and TNF α released by CAR-T cells in coculture with GSC-1 cells for indicated time points via ELISA (n = 4 technical replicates). The data depicted are one representative of three independent experiments with similar results. (D) Illustration for producing VSV Δ G*G and VSV Δ G*S recombinant viruses. HEK-293T cells were transfected with plasmid carrying G protein of VSV (pCAG-VSV-G) or spike protein of SARS-CoV-2 (pCAG-SARS-CoV2-S), respectively. Then the cells were infected with VSV Δ G*G pseudovirus for packing new VSV Δ G*G or VSV Δ G*S, respectively. (E-G) Cytotoxic measurement of CAR-T cells at different ratios (CAR-T:Tumor). B7H3–CAR-T or CR2/3–B7H3–CAR-T cells loaded with the replicative deficient viral



strain VSV Δ G*G or VSV Δ G*S. Then CAR-T cells were cocultured with GSC-1 (E), U87 (F), and LN229 (G) at indicated ratios from 0.1:1 to 3:1 (CAR-T:Tumor) for 24 h. The cytotoxicity of CAR-T cells was measured by LDH release assay (n=3 biological replicates). (H) Verification of the KO efficiency of B7H3 in U87 cells. U87 cells were infected with lentivirus carrying the sgRNA-targeting B7H3. After the puromycin (2 μ g/ml) resistance selection for 2 wk, the B7H3 expression level of U87 cells were measured by flow cytometry. (I) Cytotoxic activities of CAR-T cells preloaded with VSV Δ G*G to U87-B7H3-KO (U87-sgB7H3) cells. CAR-T and U87-B7H3-KO cells were cocultured at indicated ratio from 0.1:1 to 3:1 (CAR-T:Tumor) for 24 h (n=3 biological replicates). Data represent the mean \pm SD from three independent experiments (B, E–G, and I). Statistics by one-way ANOVA with Tukey's post hoc test (B and C) or two-way ANOVA with Bonferroni post hoc test (E–G and I). *, P < 0.05; **, P < 0.01; N.S., no significance.

Because the CAR clustering is the basis of IS formation, we next studied whether the anchored virus particles on the extracellular CR2/3-CAR moiety could induce a CAR-driven IS formation. To test this hypothesis, we added CAR antigen protein to poly-L-lysine-coated glass slides and allowed different CAR-T cells to interact with coated antigen for 30 min. We then assessed synaptic area, downstream signaling via ZAP70 phosphorylation, and lysosomal polarization via total internal reflection fluorescence microscopy (TIRFM). We found a marked difference between CR2/3-CAR-TVSV and CAR-TVSV in the synaptic area, pZAP70 accumulation, and lysosomal polarization at the IS (Fig. 5 C). The synaptic area was more condensed, and pZAP70 was increased in CR2/3-CAR-TVSV, suggesting a more efficient signaling cascade (Fig. 5 D). LAMP-1 was also elevated in CR2/3-CAR-TVSV, which suggests that cytotoxic vesicle recruitment to the IS is enhanced (Fig. 5 D). Moreover, to explore whether the specifically loaded VSVΔ51 viral particles were directly involved in the efficient formation of IS, we detected the existence of VSV-G in the IS area. We found an increased density of VSV-G at the IS of CR2/3-CAR-TVSV (Fig. 5, E and F). These data suggested that the multiple-interaction between copies of VSV-G on the viral particle and copies of extracellular CR2/3-CAR moieties (VSV-G:CR2/3-CAR) facilitated forming antigenfree CAR clusters and antigen-induced CAR synapse on CAR-T cells (Fig. 5 G).

The IS formation could help CAR-T to ameliorate chronic antigen exposure-induced T cell dysfunction (Xu et al., 2024). To assess long-term antitumor function of CAR-T, we continuously challenged CAR-T cells with multiple rounds of tumor cells in vitro. U87 cells were cultured with B7H3-CAR-T cell at 1:1 ratio, and 2 days were given for tumor elimination before the addition of another round of U87 cells (Fig. S3 A). After three rounds, CAR-T cells displayed evident exhaustion features, including impaired cell expansion (Fig. S3 B) as well as upregulation of CD39 markers (Fig. S3 C). CR2/3-CAR-TVSV cells displayed a clear advantage on delaying T cell exhaustion over CAR-TVSV and other groups (Fig. S3, B and C). On the sixth round, CR2/3-CAR-TVSV cells sustained higher level of functional activity markers, including granzyme B, TNFα, and IFNγ (Fig. S3 D). These data suggested that the VSV loading-induced CAR synapse facilitated to reduce the exhaustion under the repetitive antigen exposure and improve the persistent cytotoxicity of CR2/CR3-CAR-T cells.

Pre-activated CR2/3-CAR-T^{VSV} cells proliferated and exhibited strong metabolic and immunological activities in tumor microenvironment

To investigate the $in\ vivo$ functions of CR2/3–CAR-T $^{\rm VSV}$ after infiltrating tumor microenvironment, we first analyzed the

transcriptomic signatures at an early stage after CAR-T infiltrating into tumor tissue. We constructed the orthotopic GBM xenograft model with U87 cells, then i.v. injected CAR-T cells. 16 h after injection, CAR-T were isolated from the brain tumors for RNA sequencing (Fig. 6 A). Gene set enrichment analysis (GSEA) revealed that the signal pathway related to metabolic reprogramming and cell proliferation were significantly enriched in the CR2/3-CAR-TVSV, including MYC_targeting, mTOCRC1_signaling, and glycolysis (Fig. 6 B). Importantly, the VSVΔ51 loading on CR2/3-CAR increased the number of intratumoral CAR-T cells and Ki67 staining of CAR-T cells in vivo (Fig. 6, C and D), indicating that the increased number of intratumoral CAR-T cells was, at least partially, due to the enhancement of cell proliferation. CAR-T cells isolated from the tumor tissue were stained ex vivo with the mitochondrial dyes Mito-Tracker Deep Red and 2-NBDG. Consistent with the in vitro phenomenon, CR2/3-CAR-TVSV cells exhibited higher metabolic fitness compared with CAR-TVSV (Fig. 6, E and F). We also evaluated T cell functional activity and found that CR2/3-CAR- T^{VSV} showed a higher production of IFN γ (Fig. 6 G). To further verify whether VSV loading promotes the persistence of CR2/3-CAR-T cells in vivo, we labeled CAR-T cells with infrared fluorescent dye DiR for monitoring the CAR-T distribution in the orthotopic U87 xenograft model (Fig. 6 H). We found that abundant CAR-T signals were distributed at the brain tumor, indicating that both CR2/3-CAR-TVSV and CAR-TVSV could specifically target the intracranial tumors (Fig. 6 I). Furthermore, CR2/3-CAR-T^{VSV} group maintained stronger fluorescence signal at brain tumors compared with CAR-T^{VSV} group (Fig. 6, I and J). These data indicated that VSVΔ51 loading promoted the metabolic fitness, function activity, and the persistence of CR2/3-CAR-T cells in the tumor microenvironment.

To further verify whether this pre-activation effect driven by specific loading of viruses on CR 2/3-CAR moiety rather than the viral adsorbing onto CAR-T cell surface contributes to the potently enhanced antitumor activity, we designed three different forms of virus delivery: (1) physical increase of viral adsorption onto CAR-T cell surface via a spin-infected protocol (CAR-T^{VSV}spin infected); (2) separate delivery to CAR-T and virus (CR2/3-CAR-T + VSV i.v.); (3) specific loading of virus and CR2/3-CAR protocol (centrifugation 2,000 g for 2 h) to promote the adsorption and infection of VSV Δ 51 on the CAR-T cells at a MOI of 1, 3, 10, and 30. We found that the amount of viral adsorption of CAR-TVSV-spin infected at MOI of 10 was approximately equal to the one of CAR-T^{VSV} loading (Fig. S4, A and B). Thus, we next compared the antitumor effect of CAR-T^{VSV-spin infected} and CAR-T^{VSV} loading at MOI of 10, which exhibited a similar viral loading ability. While the treatment of CAR-TVSV-spin infected improved



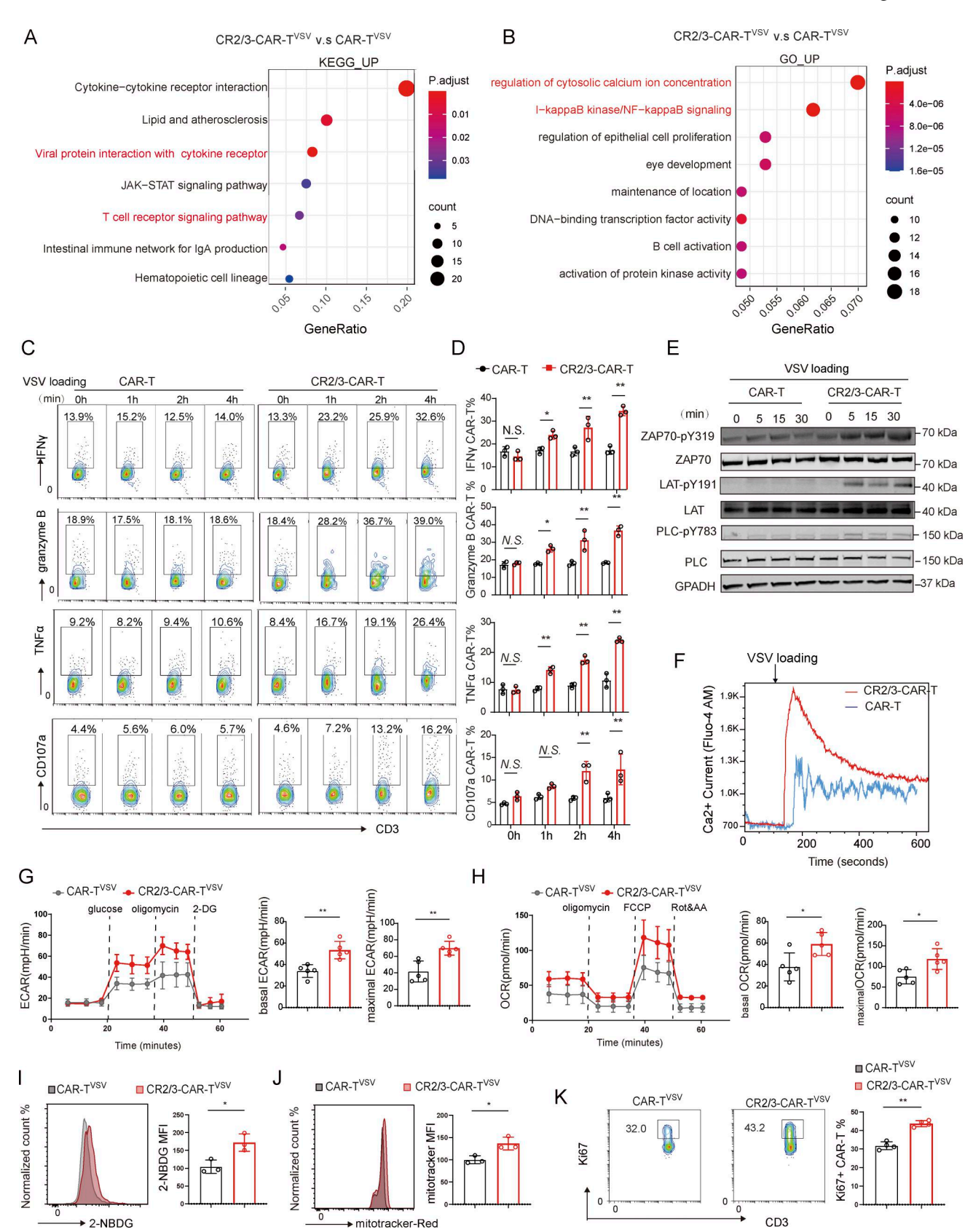


Figure 4. Specific loading of VSV viruses on CR2/3-CAR promoted the CAR signaling, metabolic fitness, and functional activity of CAR-T cells. (A and B) Transcriptome comparison between CR2/3-B7H3-CART^{VSV} cells and B7H3-CAR-T^{VSV} cells at tumor antigen-free condition (n = 3 biological replicates). Significantly enriched terms of KEGG-annotated (A) and GO-annotated (B) are shown. (C and D) Flow cytometry analysis for functional activity of CAR-T cells by measuring the expression of granzyme B, IFNy, CD107a, and TNFα after loading of VSVΔ51 (MOI = 10) for indicated time from 1 to 4 h. (C) Representative images



of flow cytometry analysis. **(D)** Quantitative data of flow cytometry analysis (n = 3 biological replicates). **(E)** Immunoblotting analysis for CAR-mediated proximal signaling. The phosphorylation of ZAP70, LAT, and PLC γ of CAR-T cells were measured after VSV Δ 51 loading (MOI = 10) at indicated times from 0 to 30 min. A representative experiment is shown, repeated twice. **(F)** Ca²⁺ influx was measured by Fluo-4 fluorescence probe in CAR-T cells. CAR-T cells were loaded with VSV Δ 51 (MOI = 10), and then the MFI of Fluo-4 was measured by flow cytometry in real time. A representative experiment is shown, repeated twice. **(G and H)** Glycolytic capacity and oxidative phosphorylation capacity of CAR-T were measured by Seahorse XF extracellular flux analyzer. ECAR (G) or OCR (H) of CAR-T cells was measured after CAR-T cells were loaded with VSV Δ 51 (MOI = 10) for 8 h (n = 4 technical replicates). The data depicted are one representative of three independent experiments with similar results. **(I)** Measurement of glucose uptake in CAR-T cells. CAR-T cells were loaded with VSV Δ 51 (MOI = 10) for 8 h, then were stained with 2-NBDG, a fluorescent derivative of glucose (n = 3 biological replicates). **(J)** Measurement of mitochondria mass in CAR-T cells. CAR-T cells were loaded with VSV Δ 51 (MOI = 10) for 8 h, then were stained with MitoTracker Deep Red (n = 3 biological replicates). **(K)** Ki67 expression of CAR-T cells was measured via flow cytometry. CAR-T cells were loaded with VSV Δ 51 (MOI = 10) for 12 h (n = 3 biological replicates). Data represent the mean n = 1 SD from three independent experiments (D and I–K) and one representative of three independent experiments (G and H). Statistics by unpaired two-tailed Student's t test (D and G–K). *, P < 0.05; **, P < 0.01; N.S., no significance. GO, gene ontology. Source data are available for this figure: SourceData F4.

the survival time of mice compared with CAR-T + VSV i.v. treatment, CAR-TVSV loading elicited the optimal therapeutic effect compared with other groups (Fig. 6 L). Bioluminescence in vivo imaging analysis also confirmed that CAR-TVSV loading showed better antitumor function in suppressing tumor growth (Fig. 6, M and N). We next evaluated the T cell exhaustion and functional activity of intra-tumor CAR-T via flow cytometry analysis (Fig. S4 C). Our data revealed that CAR-TVSV loading exhibited reduced T cell exhaustion (Fig. S4 D) and higher expression of Ki67, granzyme B, and IFN γ (Fig. S4, F and G) compared with CAR-TVSV-spin infected. These data further supported that specific loading of viruses on CR2/3-CAR moiety contribute to the potently enhanced antitumor activity.

CR2/3-CAR-T^{VSV} displayed potent antitumor activity and restrained the antigen escape *in vivo*

We next systematically evaluated the therapeutic potential of CR2/3-CAR-TVSV in vivo. The NCG mice with U87 orthotopic tumors were divided into six group and i.v. treated with (1) PBS, (2) VSVΔ51, (3) CAR-T, (4) CAR-TVSV, (5) CR2/3-CAR-T, and (6) CR2/3-CAR-TVSV. We found that CR2/3-CAR-TVSV treatment led to an improved survival time, compared with CAR-TVSV treatment or single treatment of CAR-T (Fig. 7, A and B). CR2/3-CAR-T^{VSV} treatment significantly reduced the volume of intracranial tumor (Fig. 7 C). CR2/3-CAR-TVSV treatment also showed a higher production of cytokines (Fig. 7 D) and reduced the coexpression of the inhibitory receptors PD-1, TIM-3, and LAG-3 on CAR-T (Fig. 7 E). It is notable that CR2/3-CAR-T^{VSV} treatment was well tolerated with no change in mice weight (Fig. S5 A), no systemic cytokine release (IL-6 and TNFα), and no liver or kidney injury detected (Fig. S5, B and C). There was also no significant abnormal pathologic change in vital tissues (Fig. S5 D). These results indicated the strong antitumor efficacy and safety of CR2/3-CAR-TVSV in vivo.

CAR antigen downregulation or loss, or baseline heterogeneous expression, could lead to therapeutic escape (Khong and Restifo, 2002). Induction of CAR-driven mature ISs could improve antigen sensitivity and help to overcome the tumor antigen escape (Xu et al., 2024). We further asked if our strategy could help to restrain the antigen escape *in vivo* and generated an orthotopic tumor model composed of a mixed population with increased tumor antigen heterogeneity (20% U87-B7H3-KO cells and 80% U87-WT cells) (Fig. 7 F). We demonstrated that, while a single treatment of CAR-T cells did not improve the survival

time of mice, the CR2/3–CAR-T^{VSV} treatment led to improved survival time of mice compared with CAR-T^{VSV} treatment (Fig. 7 G). Bioluminescence *in vivo* imaging analysis also confirmed that CR2/3–CAR-T^{VSV} treatment inhibited the tumor growth of intracranial xenograft, compared with the other groups (Fig. 7, H and I). These data indicated that CR2/3-CART^{VSV} help to restrain the antigen escape and overcome therapeutic resistance.

We next test whether this CR2/3–CAR-T^{VSV} strategy could be generalized to other tumor types. The breast cancers model was established by subcutaneously implanting with 3 \times 10⁶ MDA-MB-231 cells into NCG mice (Fig. 7 J). We found that the treatment of VSV or CAR-T cells only slightly delayed the tumor growth (Fig. 7, K and L). However, CR2/3-B7H3-CAR-T^{VSV} markedly reduced tumor growth and tumor burden of MDA-MB-231 xenograft compared with CAR-T^{VSV} treatment or other treatment groups (Fig. 7, K and L). These data supported that CR2/3-CART^{VSV} strategy can be adopted for several solid tumors, including glioma and breast cancers.

Discussion

CAR-T cell therapy and oncolytic virotherapy are complementary modalities that show remarkable benefits and encouraging results for solid tumor treatment (Chen et al., 2024; Evgin et al., 2022; Zheng et al., 2022). For the combination of CAR-T cells and oncolytic virotherapy, a key issue is to formulate and optimize the combination of two agents. In this study, we initially attempted to increase specific loading of OV VSV Δ 51 onto the cell surface of CAR-T cells. While we successfully achieved an approximately fivefold increase in specific viral loading and more effectively delivering OVs into tumor sites, we observed that CAR-T cells were pre-activated via cross-connection between viral particles and CR2/3-CAR moieties and induction of an unexpected IS formation on the surface of CAR-T cells (Fig. 5 G).

Previous studies indicate that co-delivery strategies shorten the spatiotemporal distance between OV and CAR-T, enhancing their synergistic effects. In 2022, Zheng et al. utilized centrifugation to preinfect CAR-T cells with OVs (Zheng et al., 2022). This strategy enhanced viral perfusion efficiency within tumors while inducing spontaneous tumor cell death and suppressing antigen escape. However, OV infection led to proliferation suppression and functional exhaustion of CAR-T cells. To balance efficacy and toxicity of this loading approach, the team



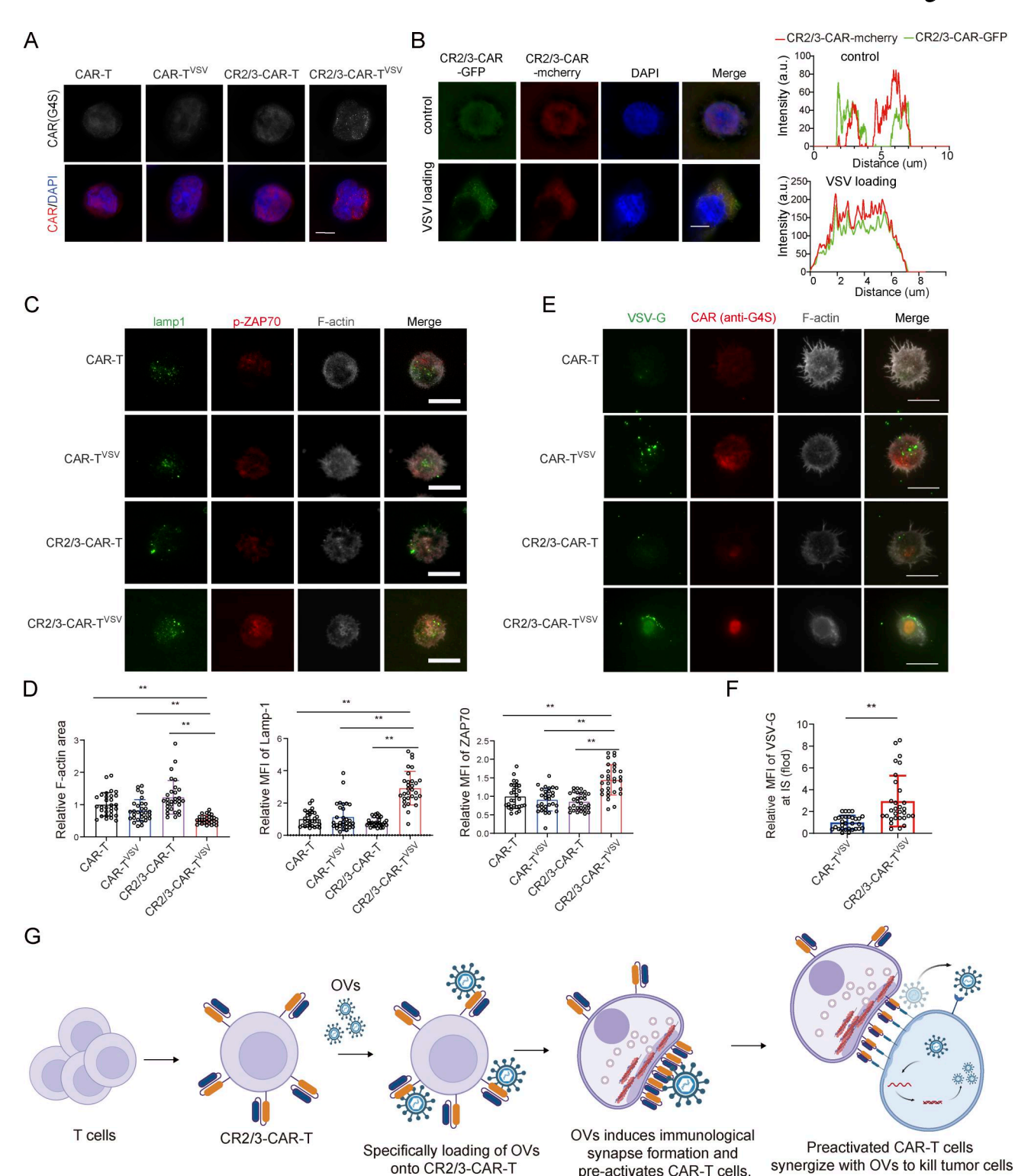


Figure 5. Loading of VSVΔ51 induced CAR clustering and synapse formation on CR2/3-CAR-T cells. (A) Super-resolution imaging analysis of CAR clustering in CAR-T. B7H3-CAR-T cells were loaded with VSVΔ51 (MOI = 10) for 30 min, then the CAR micro-clusters were detected using anti-G4S Ab. Scale bar, 5 μm. (B) Super-resolution imaging analysis of co-localization of mcherry-CR2/3-CAR and GFP-CR2/3-CAR in CR2/3-CAR-T cells. CR2/3-B7H3-CAR-T cells were co-transfected with mcherry-CR2/3-CAR and GFP-CR2/3-CAR and loaded with VSVΔ51 (MOI = 10) for 30 min, then the co-localization of CAR was measured. Scale bar, 5 μm. (C-F) TIRFM analysis of IS of B7H3-CAR-T cells on stimulatory recombinant human B7H3 protein coated on glass slides. (C) Representative images for lamp1 (green), pZAP70 (red), and F-actin (white) at IS. (D) Quantified fluorescent data of synapse area and MFI of lamp1 and pZAP70 are shown (n = 30 cells from three independent experiments). (E) Representative images for VSV-G (green), CAR (red), and F-actin (white) at IS. (F) Quantified fluorescent data of viral protein VSV-G are shown (n = 30 cells from three independent experiments). Scale bar, 10 μm. (G) Scheme of loading of OV VSVΔ51 on CR2/3-CAR moiety, which pre-activates CAR-T cells and induces more efficient formation of IS. Data represent the mean ± SD from three independent experiments (D and F). A representative experiment is shown, repeated at least twice (A-C and E). Statistics by one-way ANOVA with Tukey's post hoc test (D and F). *, P < 0.05; **, P < 0.01; N.S., no significance.



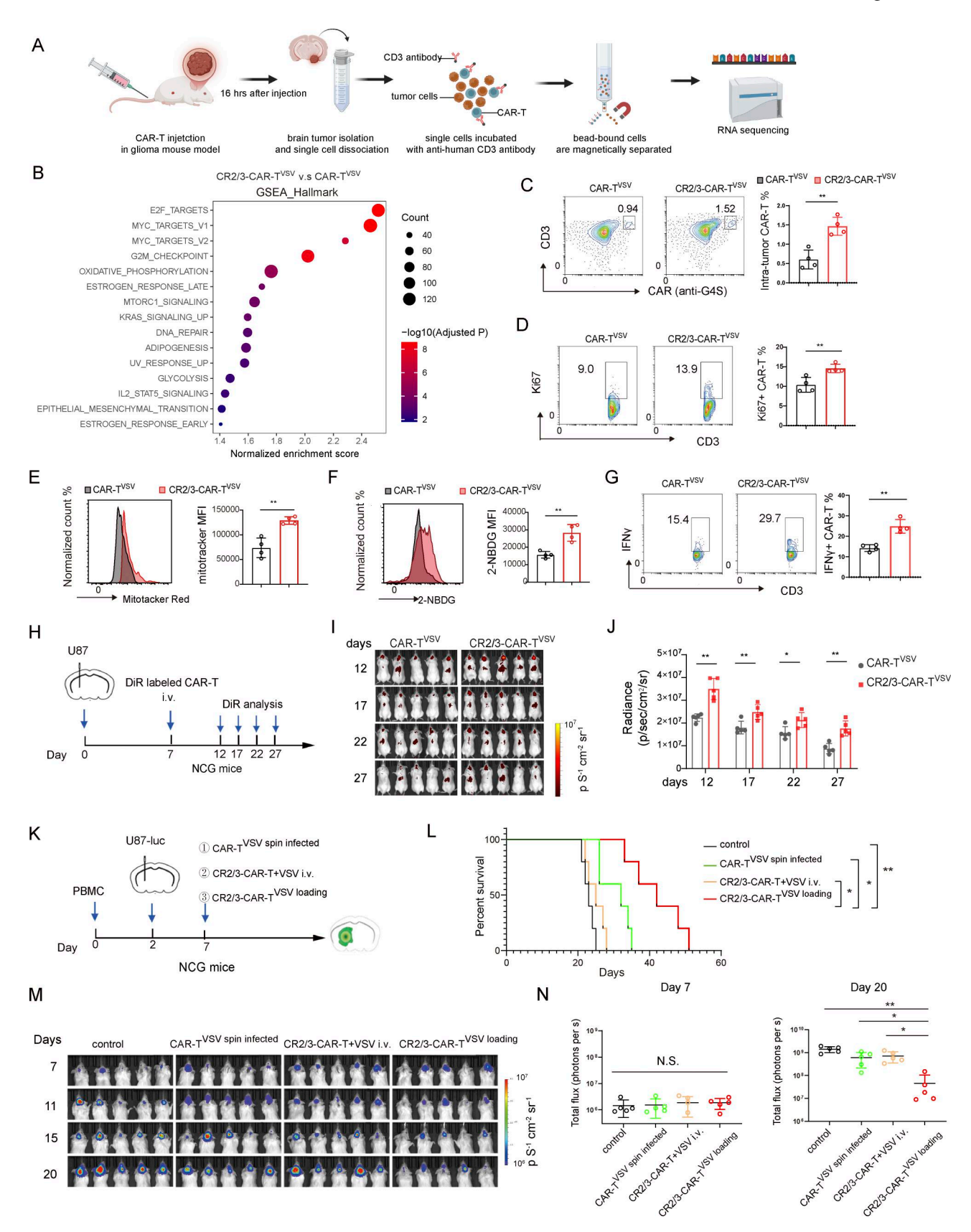


Figure 6. **Pre-activated CR2/3–CAR-T^{VSV} cells proliferated and exhibited strong metabolic and immunological activities in tumor microenvironment. (A)** Diagram depicting transcriptome analysis of intra-tumor CAR-T cells. NCG mice bearing U87 intracranial xenograft were injected with B7H3–CAR-T^{VSV} (5 × 10^6 cells) and CR2/3–B7H3–CAR-T^{VSV} (5 × 10^6 cells). 16 h after the injection, CAR-T cells were isolated via magnetic bead-bound Ab against CD3. **(B)** GSEA for CAR-T cells isolated from A. The top 15 enriched pathways in CR2/3–B7H3–CAR-T^{VSV} group were presented compared with B7H3–CAR-T^{VSV} group (n = 3).



biological replicates). **(C-G)** Flow cytometric analysis of intra-tumor CAR-T cells in A. The ratios of intra-tumor CAR-T cells (C), Ki67 expression (D), mitochondria mass (E), glucose uptake (F), and IFNy expression (G) of CAR-T cells were analyzed (n = 4 biological replicates). **(H)** Scheme of the experimental design for analyzing the CAR-T persistence *in vivo*. CAR-T cells were labeled with DiR (5 μ M) and then were loaded with VSV (MOI = 10). CAR-T cells were injected 7 days after tumor implantation. **(I)** Representative fluorescence images of tumor-bearing mice for measuring the distribution of DiR-labeled CAR-T cells. **(J)** Quantitative analysis of fluorescence images (n = 5 mice). **(K)** Diagram depicting generation of antigen heterogeneity glioma model and CAR-T treatment schedule. VSV Δ 51 was combined with CAR-T cells in three different forms for virus delivery: (1) physical increase of viral adsorption onto CAR-T via a spin-infected protocol (CAR-TVSV-spin infected), (2) separate delivery to CAR-T and virus (CAR-T + VSV i.v.), and (3) specific loading of virus and CR2/3-CAR (CAR-TVSV loading). CAR-T cells and VSV Δ 51 were i.v. injected at 7 days, and flow cytometry was performed at 14 days. **(L)** Kaplan–Meier survival curve of mice bearing U87^{20%} B³H3-KO intracranial tumors (n = 5 mice). **(M and N)** Monitoring of tumor progression via bioluminescence imaging of luciferase in U87 xenograft mice at indicated time. **(M)** Representative bioluminescence images of U87 intracranial tumor after treatment. **(N)** Quantitative analysis of tumor bioluminescence data (n = 5 mice per group). Data represent the mean \pm SD from one of two independent experiments (C = 6, D = 6,

administered a mixture of 10% preinfected CAR-T cells and 90% regular CAR-T cells. In 2024, Chen et al. developed the Oncotech technology (Chen et al., 2024). This approach coats oncolytic adenovirus with a biomembrane, which is then conjugated to T cells to form virus-T cell chimeras, significantly improving the co-delivery efficiency of OVs. However, the requirement to coat the virus before loading it onto T cells introduces complex manufacturing steps that may hinder clinical translation. The existing co-delivery approaches have limitations, including T cell exhaustion induced by the random viral infection of OVs, and complex biomembrane coating processes impede clinical translation. In this study, we develop a simplified and efficient method for CAR-T/OV co-delivery strategies.

The IS formation is important for a cell-cell contact between TCR and peptides displayed by MHC on the surface of antigenpresenting cells or target cells (Hammer et al., 2019). Within T cells, the signaling machinery—comprising kinases, cytoskeletal elements, adhesion molecules, and organelles-is intrinsically organized along a polarized TCR axis (Liu et al., 2009). In addition, it directs the polarized secretion of cytokines, other functional molecules, and even bioactive microvesicles (Li et al., 2024; Orange, 2008). Although it has been shown that the CAR: antigen complexes only form disordered synapses in CAR-T cells, we found that the cross-connection between multiple copies of VSV-G protein on a viral particle and CR2/3-CAR moieties on the surface of CAR-T cells induce the aggregation of CAR-T moieties and IS formation, which subsequently preactivate CAR-T cells before contacting with target cells (Fig. 5 G). This pre-activation is short-lived and moderate, which would not lead to overstimulation and cause cell exhaustion. In contrast, the pre-activated CAR-T cells could generate positive proximal signals to create a status, which could effectively resist the activation of intrinsic immunity and resist to the exhausting signals in intracellular environment brought by OVs attachment. Moreover, the pre-activated CAR-T cells proliferate and exhibit strong metabolic and immunological activities and more effectively prevent different suppressive influences in tumor microenvironment.

Our current study does present some limitations. First, the generalization of our strategy to other solid tumor types requires validation. It also remains unknown whether the approach of inserting viral receptor fragments into the CAR for virus loading could be feasible for other OV strains. Second, further investigation is needed to determine if this strategy improves viral

delivery in immunocompetent models. Both adaptive and innate immune systems rapidly eliminate circulating viruses. Critically, the neutralizing Abs generated upon repeated administration could potentially neutralize virions anchored to CAR-T cell membranes. Third, it is necessary to develop a simplified premixed formulations for CAR-T cells loading with OVs. Current procedure requires viral loading and centrifugation of CAR-T, which is not feasible to manipulate for clinical use.

Our study reveals a novel mechanism for the formation of functional IS and suggests that the pre-activation of CAR-T cells can be further explored as a potent modality to enhance their antitumor effect. Importantly, we provide a solid method for inserting the binding domain of viral receptor into CAR moiety to simultaneously facilitate much more specific loading of OVs onto CAR-T cells and pre-activate the CAR-T cells. Therefore, this strategy potently promotes the synergetic effect of combining OVs and CAR-T cells for treating solid tumors, at least GBM.

Materials and methods

Cell lines and virus

The human GBM cell lines U87, LN229, and U251 were purchased from the American Type Culture Collection. The GBM cell lines were maintained at 37°C under 5% CO₂ in high glucose DMEM (Gibco) supplemented with 10% Australian FBS (Gibco). Primary patient-derived glioma stem cells (GSC-1) were provided by Prof. Guangmei Yan (Sun Yat-sen University, Guangzhou, P.R. China) (Xing et al., 2017). The primary patient-derived GSCs were cultured under clonal conditions in low-adherence plates (3471; Corning) and maintained in DMEM/F12 medium (11320033; Gibco) supplemented with 2% B27 (17504044; Gibco), 20 ng/ml basic FGF (100-47; PeproTech), and 10 ng/ml EGF (100-47; PeproTech) at 37°C under 5% CO₂. Tumor spheres were reseeded every 4 days after dissociation with accutase (A6964; Innovative Cell Technologies). The OV VSVΔ51 provided by Prof. Devin Guo (Guangzhou National Laboratory, Guangzhou, P.R. China) was replicated and amplified in Vero cells (Xiao et al., 2022).

To construct recombinant VSV carrying luciferase, the coding sequences were inserted into VSV backbone between the VSV glycoprotein (G protein) and polymerase protein (L protein) using NheI (ER0972; Thermo Fisher Scientific) and XhoI (ER0691; Thermo Fisher Scientific) restriction enzyme sites. The VSV backbone harbors an M51R substitution in the matrix (M)



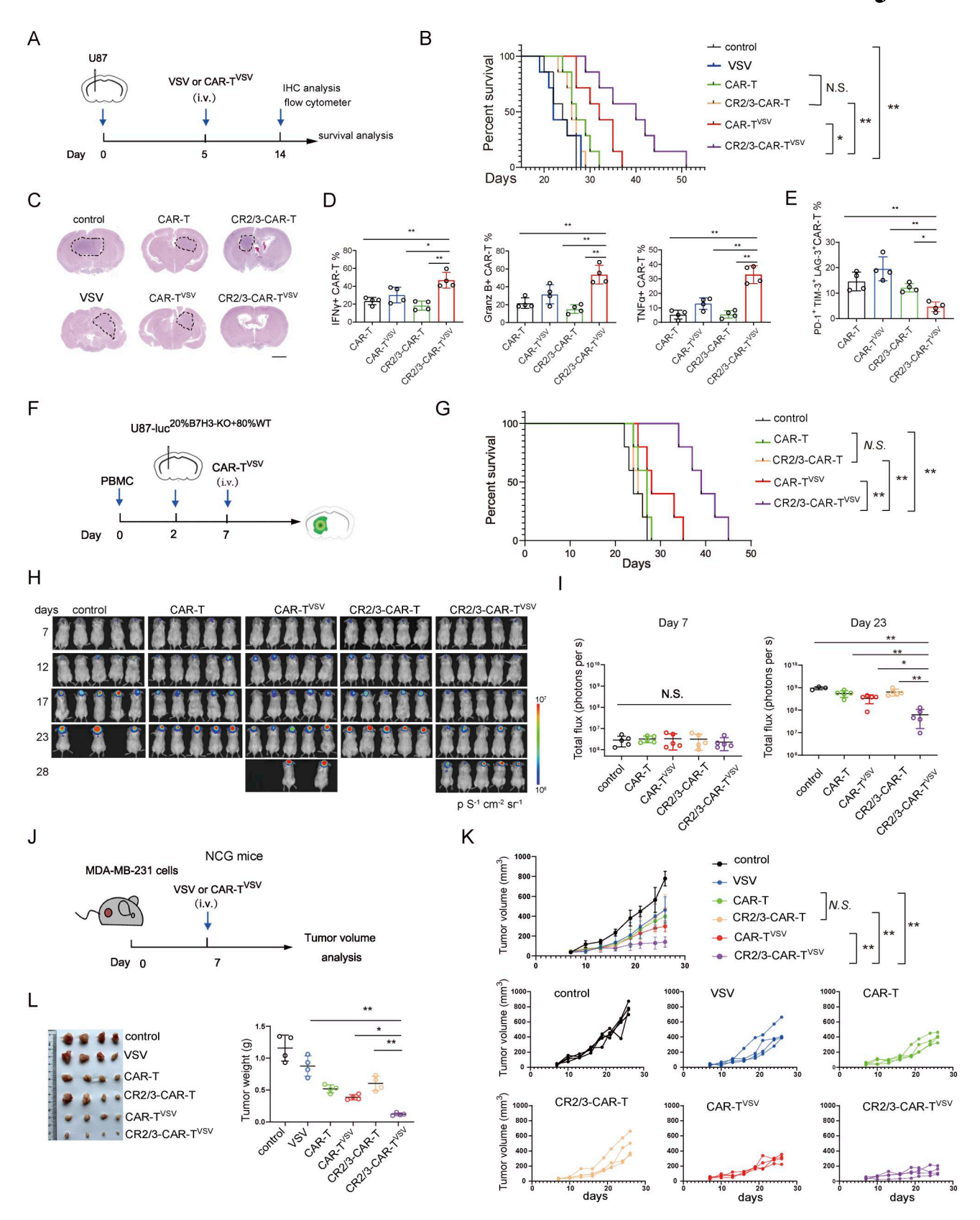


Figure 7. **CR2/3–CAR-T^{VSV} displayed potent antitumor activity and restrained the antigen escape** *in vivo.* **(A)** Diagram depicting the CAR-T treatment schedule in the mice bearing U87 intracranial tumors. U87 cells were inoculated into the mouse brain at day 0. CAR-T cells were injected at 5 days. Flow cytometry analysis was performed at 14 days. **(B)** Survival time of NCG mice bearing U87 intracranial xenograft (n = 7 mice). The mice were i.v. treated with VSV Δ 51 (2×10^6 PFU), B7H3–CAR-T (10^6 cells), CR2/3–B7H3–CAR-T(10^6 cells), B7H3–CAR-T^{VSV}(10^6 cells), and CR2/3–B7H3–CAR-T (10^6 cells). **(C)** H&E staining of mouse brain sections from A was performed at 14 days. Scale bar, 1 cm. **(D and E)** T cell exhaustion and functional activity of CAR-T cells were



analyzed in brain tumor tissue by measuring intracellular expression cytokines granzyme B, TNFα, and IFNγ (D) and the co-expression of the exhaustion markers PD-1, TIM-3, and LAG-3 (E) via flow cytometry (n = 4 biological replicates) at 9 days after CAR-T cell injection. (**F**) Diagram depicting the generation of antigen heterogeneity glioma model and CAR-T treatment schedule in the mice bearing mixed U87 intracranial tumors (20% B7H3-KO cells + 80% B7H3-WT cells). NCG mice were i.v. injected with 3×10^6 PBMCs at day 0. After 2 days, 20% B7H3-KO- and 80% B7H3-WT-mixed U87 cells (3×10^5 total cells per mouse) were injected into the mouse brain. CAR-T cells, loaded with VSVΔ51 or not, were i.v. injected at 7 days. (**G**) Kaplan-Meier survival curve of mice bearing U87^{20%} B7H3-KO intracranial tumors (n = 5 mice). (**H and I**) Monitoring of tumor progression via bioluminescence imaging of luciferase in U87 xenograft mice at the indicated time (n = 5 mice). (**H**) Representative bioluminescence images of U87 intracranial tumor after treatment. (**I**) Quantitative analysis of tumor bioluminescence data. (**J**) Diagram depicting the generation breast cancer model and CAR-T treatment schedule in the mice bearing subcutaneous MDA-MB-231 cells tumors. Breast cancer cells, MDA-MB-231 cells (3×10^6 total cells per mouse), were injected into the mice. CAR-T, loaded with VSVΔ51 or not, were i.v. injected at 7 days. (**K**) Tumor volume was recorded every 3 days (n = 4 mice). (**L**) Representative images and weights of tumor xenografts at the end of the experiment (n = 4 mice). Data represent the mean \pm SD from one of two independent experiments (B, G, D, E, I, L, and K). Statistics by log-rank Mantel-Cox tests (B and G), one-way ANOVA with Tukey's multiple comparison test (D, E, I, and L), and two-way ANOVA (K). *, P < 0.01; N.S., no significance.

gene, attenuating the neural virulence of the original strain. The recombinant viruses (VSV-luciferase) were recovered in Vero E6 cells.

To construct recombinant VSV ΔG^*G or VSV ΔG^*S , the backbone of the pseudotyped virus comes from the VSV virus, in which the G gene is deleted (VSV ΔG), and the G protein from VSV or S protein from SARS-CoV-2 is incorporated as the membrane protein from another plasmid in trans (Nie et al., 2020). The recombinant VSV ΔG^*G and VSV ΔG^*S were recovered in 293T cells, which were transfected with the plasmid carrying G protein from VSV or S protein from SARS-CoV-2, respectively.

Isolation and culture of primary human T lymphocytes

Peripheral blood mononuclear cells (PBMCs) were derived from samples obtained from healthy volunteers from anonymous buffy coats of donors (Guangzhou Blood Center, Guangzhou, P.R. China) by Ficoll-Hypaque gradient separation. Primary human CD3+ T cells were positively purified with magnetic beads to a purity of >98% from PBMCs with an enrichment set (STEMCELL). T lymphocytes were activated by anti-CD3 (R&D Systems) and anti-CD28 (R&D Systems) Abs at 1 $\mu g/ml$. The transduced T cells were expanded in the conditioned medium containing 90% RPMI 1640 (Gibco; Invitrogen) supplemented with 10% FBS (Gibco; Invitrogen), 0.1 mM nonessential amino acids (Gibco; Invitrogen), 2 mM GlutaMAX (Gibco; Invitrogen), and 0.05 mM 2-mercaptoethanol at an initial concentration of 1×10^6 cells per ml. Cells were fed twice a week with recombinant IL-2 (10 ng/ml) (R&D Systems).

Construction of CAR-encoding lentiviral vector

The anti-EGFR single-chain fragment variable (scFV) was derived from the basic sequence of cetuximab. The anti-B7H3 scFv was derived from mAb 376.96 (Du et al., 2019; Fauci et al., 2014). IL13R α 2-specific CAR recognizes IL13R α 2 via a membrane-tethered IL13 ligand mutated at a single site (E13Y) (Brown et al., 2015). The scFv region was fused with CD8a transmembrane domain and intracellular domains, which contain CD28 (nucleotides 460–660; NM_006139.3), 4-1BB (nucleotides 640–765; NM_001561.5), and CD3 ζ (nucleotides 160–492; NM_198053.2) in tandem with GGGGS sequences inserted between each domain. The sequence of two distinct CR domains of LDLR (NM_000527.5), which serve as a major binding domain for VSV, was ligated to the CAR structure in five ways constructed to

form the CARs (Nikolic et al., 2018). Sequences of CR domains were listed below. Truncated CD19 (nucleotides 1–960; NM_001178098.2) was ligated to the 2A peptides derived from porcine echovirus-1 (P2A). The sequences of CR2 and CR3 domain of LDLR were as follows:

CR2 domain

5'-TGCAAATCCGGGGACTTCAGCTGTGGGGGGCCGTGTCAAC CGCTGCATTCCTCAGTTCTGGAGGTGCGATGGCCAAGTGGAC TGCGACAACGGCTCAGACGAGCAAGGCTGT-3'.

CR2 domain

5'-TGCTCCCAGGACGAGTTTCGCTGCCACGATGGGAAGTGC ATCTCTCGGCAGTTCGTCTGTGACTCAGACCGGGACTGCTTG GACGGCTCAGACGAGGCCTCCTGC-3'.

CR2/CR3 (CR2/3) domain

5'-TGCAAATCCGGGGACTTCAGCTGTGGGGGCCGTGTCAAC CGCTGCATTCCTCAGTTCTGGAGGTGCGATGGCCAAGTGGAC TGCGACAACGGCTCAGACGAGCAAGGCTGTCCCCCCAAGACGT GCTCCCAGGACGAGTTTCGCTGCCACGATGGGAAGTGCATC TCTCGGCAGTTCGTCTGTGACTCAGACCGGGACTGCTTGGAC GGCTCAGACGAGGCCTCCTGC-3'.

Lentivirus-mediated gene transfer

The main procedures were conducted as previously described (Qiao et al., 2023). The core vector, packing plasmids psPAX2, and the envelope plasmid pMD2.G were co-transfected into HEK293T cells using polyethyleneimine. The medium was changed 8 h after transfection. 48 h after transfection, cell supernatants containing lentivirus were collected and passed through a 0.45-µm filter.

For CAR-T cell generation, the activated CD3 $^{+}$ T lymphocytes were transduced with lentiviral supernatants using RetroNectin-coated plates, with polybrene (TR-1003-G; Sigma-Aldrich) at 8 μ g/ml, followed by centrifugation for 60 min at 500 g, then incubated at 37 $^{\circ}$ C. 12 h later, the recombinant viruses were removed, and T cells were expanded in the conditioned medium as described above. The genetically modified T cells were maintained in a complete T cell medium in the presence of IL-2 (fed twice a week, 10 ng/ml) and used for functional assay 14 days after transduction.

For CRISPR/Cas9-mediated gene KO of B7H3, human B7H3 sgRNA was designed and constructed using a lentiCRISPRv2



vector by the company (MiaoLing Biology). Lentivirus carrying B7H3 sgRNA was constructed as described above. A CRISPR-Cas9 vector with nontargeting sgRNA was used as the control.

For stable cell line construction, U87 cells were introduced with lentivirus for 8 h. 48 hrs after introduction, the cells were selected with 2 μ g/ml puromycin for 7–10 days to establish stably expressing cell lines. For animal models, U87 cell carrying luciferase (U87-luc) was selected to establish a xenograft model in mice.

Abs and reagents

The Abs used for immunoblotting and immunohistochemistry were as follows: Phospho-Zap-70 (Tyr319)/Syk (Tyr352) Antibody (2701; Cell Signaling Technology), ZAP-70 Rabbit mAb (#3165; Cell Signaling Technology), Phospho-LAT (Tyr191) Antibody (#3584; Cell Signaling Technology), LAT Rabbit mAb (#45533; Cell Signaling Technology), PLCγ1 Rabbit mAb (#5690; Cell Signaling Technology), Ki-67 (1:400, #9449; Cell Signaling Technology for IHC), cleaved-Caspase-3 (1:500, 9664s; Cell Signaling Technology for IHC), Anti-Rabbit IgG (H+L), Alexa Fluor 647 Conjugate (1:500, 4414; Cell Signaling Technology), Pierce Goat Anti-Mouse IgG, (H+L), Peroxidase Conjugated (1:5,000, 31430; Thermo Fisher Scientific), Pierce Goat Anti-Rabbit IgG, (H+L), and Peroxidase Conjugated (1:5,000, 31460; Thermo Fisher Scientific).

Multicolor flow cytometry analysis

Brain tumor quadrants were harvested, minced, incubated with a Brain Tumor Dissociation Kit (130-095-942; Miltenyi), triturated, passed through a 70-µm screen, resuspended in HBSS, and stained with fluorochrome-conjugated anti-mouse Abs from BioLegend or eBioscience, as well as appropriate isotype control Abs. A Zombie Red Fixable viability kit (BioLegend) was used to stain dead cells. A "no-wash" sequential staining protocol (Bio-Legend) was followed to stain dead cells and for surface staining. Intracellular staining was performed following the FoxP3 intracellular staining protocol (BioLegend). For single-color compensation controls, UltraComp eBeads (eBioscience) were used and stained with each fluorescently conjugated Ab according to the manufacturer's instructions. All samples were run in a Cytoflex flow cytometer. Data were analyzed with CytExpert software. Technicians acquiring and gating the data were blinded to the treatments.

The Abs for flow cytometer analysis were as follows: APC anti-human/mouse Granzyme B Recombinant (372204; Bio-Legend), PE anti-human IFN- γ (502509; Bio-Legend), PE-Cyanine7 anti-human Ki67 (25-5698-82; eBioscience) PE-Cyanine7 anti-human TNF- α (502930; Bio-Legend), PE anti-human CD223 (LAG-3) (369306; Bio-Legend), APC anti-human CD366 (Tim-3) (369306; Bio-Legend), PE anti-human CD223 (LAG-3) (345012; Bio-Legend), PE/Cyanine7 anti-human CD279 (PD-1) (329918; Bio-Legend), Anti-(G4S)n (B02H1)mAb(FITC) (hys-bio, GS-ARFT100), and FITC anti-human CD3 (317306; Bio-Legend).

For 2-NBDG uptake assay, CAR-T cells were harvested and incubated in glucose-free medium containing 100 μ M 2-NBDG (Invitrogen) for 2 h at 37°C. For MitoTracker Deep Red staining, CAR-T cells were harvested and incubated in DPBS containing

0.5% FBS and 200 nM MitoTracker Deep Red (Invitrogen) for 30 min at room temperature. After a live/dead staining, samples were recorded on a CytoFLEX and analyzed with FlowJo.

Immunofluorescence assay

An immunofluorescence assay was performed as previously described (Chen et al., 2023). Briefly, cells were fixed with 4% poly-formaldehyde at room temperature for 20 min, then permeabilized with 1% Triton X-100 in PBS for 15 min, followed by washing three times with PBS. Cells were blocked with 5% BSA in PBS for 45 min, followed by washing three times with PBS with 0.1% Tween-20 (PBST). Blocked samples were subjected to sequential incubation with specific primary Abs and fluorescently labeled secondary Abs at room temperature for 45 min. After incubation, cells were washed with PBST three times. Cells were treated with a DAPI solution at room temperature for 10 min, followed by washing three times with PBST.

For structured illumination microscopy (SIM) imaging, CART cells were seeded in slide chambered coverslips (80826; ibidi) and attached by Cell-Tak Cell and Tissue Adhesive (354240; CORNING). Primary Abs with their dilutions are as follows: anti-VSV-G (1:100; EB0010; Kerafast) and anti-G4S (1:50; GS-ARNC25; HyCell). The original images were acquired and reconstructed to form the SIM image. All the SIM images were analyzed with the N-SIM module of the NIS-Elements AR software (Nikon).

For TIRFM imaging, antigen-coated coverslips were prepared using N1 coverslips (12-545-80P; Thermo Fisher Scientific), which were coated with 0.5 µg/ml of human B7H3 (CK62-10 ug; Novoprotein) or poly-l-lysine (P4707; Sigma-Aldrich) for 4 h. Then, they were washed with PBS and filled with media until CAR-T cell seeding. Next, CAR-T cells were plated onto the precoated coverslips for 30 min. All the primary Abs were incubated at 4°C overnight. Primary Abs and probes with their dilutions are as follows: anti-LAMP1 (1:100; #15665; Cell Signaling Technology), anti-p-ZAP70 (1:50; #2701; Cell Signaling Technology), phalloidin-Alexa Fluor 647 (1:200; A22287; Thermo Fisher Scientific), anti-VSV-G (1:100; EB0010; Kerafast), and anti-G4S (1: 50; GS-ARNC25; HyCell). Finally, cells were washed with permeabilization buffer and PBS before letting them dry for 1 h at room temperature. The original images were acquired via the TIRFM image. All the TIRFM images were analyzed with the Nikon software.

Immunohistochemistry assay

The expression of VSV-G in the tumors was assessed by immunohistochemistry. Briefly, tumor sections (4 μm) were dewaxed in xylene, hydrated in decreasing concentrations of ethanol, immersed in 0.3% H_2O_2 -methanol for 30 min, washed with PBS, and probed with mAbs or isotype controls at $4^{\circ}C$ overnight. After being washed, the sections were incubated with biotinylated goat anti-rabbit or anti-mouse IgG at room temperature for 2 h. Immunostaining was visualized with streptavidin/peroxidase complex and diaminobenzidine, and sections were counterstained with hematoxylin. The immunohistochemistry assay was made in a blinded manner for pathologists.



Repetitive stimulation assay

U87 tumor cells were seeded in complete DMEM medium 1 day prior to coculture. The next day, DMEM medium was replaced with T cell medium, and CAR-T cells were seeded on top of the tumor cells at a 1:1 E:T ratio with IL-2 at 50 IU ml $^{-1}$. Subsequent repeated cocultures were set up every 48 h. For each coculture, CAR-T cells were collected and counted using the cell counter and replated onto fresh target tumor cells at a 1:1 E:T ratio (the highest cell number among the experimental groups). This process was repeated for six rounds. CAR-T cells were collected, purified, and counted, and then were analyzed for the expression of CD39, granzyme B, IFN γ , and TNF α via flow cytometry.

Animal models

We used NCG (NOD/ShiLtJGpt-Prkdcem26Cd52Il2rqem26Cd22/Gpt, Najing GemPharmatech Co., Ltd) mouse model to assess the in vivo antitumor effect of transduced CAR-T cells. The orthotopic intracranial xenograft model was implanted stereotactically into the striatum (2.2 mm lateral from the bregma and 2.5 mm deep) to generate intracranial tumors. The U87 cells stably expressing luciferase (3 \times 10⁵ cells) were dissociated in 5 μ l of PBS. Indicated days after tumor implantation, the mice were randomly divided into groups and treated with CAR-T cells (106 cells) and/or VSVΔ51 (2 \times 10⁶ PFU) by tail vein injection. For mouse bioluminescence imaging, mice implanted with U87 cells expressing luciferase were injected intraperitoneally with a luciferin solution (15 mg/ml in DPBS, dose of 150 mg/kg). The bioluminescence images were acquired using the IVIS Lumina system and analyzed by Living Image software. Imaging experiments were conducted at the Animal Imaging platform of the Experimental Animal Center of Guangdong People's Hospital.

To evaluate the biodistribution of CAR-T cells, the CR2/3-CAR-T or normal CAR-T were pre-stained with DiR (HY-D1048; MedChemExpress) and then loaded with oncolytic VSV (MOI = 10) and washed with PBS for three times to remove unbound dyes and virus. The fluorescence images were acquired using the IVIS fluorescent system and analyzed by Living Image software.

Quantitative RT-PCR (qRT-PCR)

Total RNA was extracted with TRIzol reagent (Invitrogen). A reverse transcription system (TAKARA) was used to synthesize cDNA. SuperReal PreMix SYBR Green (AG) and an ABI Q5 Detection System were used for qRT-PCR. The mRNA results were normalized to GAPDH expression. The sequences of primers were as follows:

hGAPDH-forward: 5'-ATGACATCAAGAAGGTGGTG-3'
hGAPDH-reverse: 5'-CATACCAGGAAATGAGCTTG-3'
VSV-G-forward: 5'-GCGGGTCTTCCAATCTCTCC-3'
VSV-N-forward: 5'-TGATAGTACCGGAGGATTGACGAC-3'
VSV-N-reverse: 5'-CCTTGCAGTGACATGACTGCTCTT-3'
hIFNB1-forward: 5'-AGGACAGGATGAACTTTGAC-3'
hIFNB1-reverse: 5'-TGATAGACATTAGCCAGGAG-3'
hCXCL10-forward: 5'-GCTCTACTGAGGTGCTATGTTC-3'
hCXCL10-reverse: 5'-GGAGGATGGAAGTC-3'

hISGI5-forward: 5'-GAGAGGCAGCGAACTCATCTT-3' hISGI5-reverse: 5'-CCAGCATCTTCACCGTCAGG-3'

Immunoblot analysis

For immunoblot analysis, whole-cell extracts were collected and lysed in radioimmunoprecipitation assay lysis buffer containing 50 mM Tris-HCl, pH 8.0, 150 mM NaCl, 1.0% (vol/vol) Triton X-100, 1.0% sodium deoxycholate, and 0.1% SDS. The lysates were subjected to SDS-PAGE, transferred onto 0.45- μ m PVDF membranes, and then blotted with the indicated Abs.

Cytotoxicity assay

The ability of T cells to kill tumor target cells was measured by lactate dehydrogenase (LDH) release assay. Briefly, CAR-T cells were cocultured with target cells at different ratios (from 3:1 to 0.3:1) for 24 h in a 96-well plate (V bottom). Then LDH release was measured by the CytoTox96 nonradioactive cytotoxicity assay (G1781; Promega) according to the manufacturer's instructions. Absorbance values of wells containing effector cells alone and target cells alone were detected and subtracted as the background from the values of the cocultures. Wells containing target cells alone were mixed with a lysis reagent for 30 min at 37°C, and the resulting luminescence was set as 100% lysis. Cytotoxicity was calculated by using the following formula: % Cytotoxicity = (Experimental - Effector spontaneous - Target spontaneous)/ (Target maximum - Target spontaneous) × 100%.

Electron microscopy

CAR-T cells were preloaded with VSV Δ 51 (10 MOI). CAR-T cells were collected by centrifugation at 1,000 g for 5 min at room temperature. Cell pellets were then resuspended, washed once with PBS, pelleted at 1,500 g for 5 min, and fixed on ice for 4 h in 0.1 mol/l PBS (pH 7.4) containing 2.5% glutaraldehyde and 2% paraformaldehyde. Samples were then submitted to the Servicebio Company for scanning electron microscope analysis.

RNA sequencing and transcriptome data analysis

B7H3-CAR-T or CR2/3-B7H3-CAR-T cells were loaded with VSV Δ 51 (10 MOI) or not, then incubated without contacting target tumor cells for 3 h. Total RNA was extracted from B7H3-CAR-T or CR2/3-B7H3-CAR-T using the TRIzol reagent (Life Technologies). Samples were sent to Beijing Genomics Institute for RNA sequencing analysis. Functional analysis of differentially expressed genes was performed by gene ontology.

Viral titer measurement

For plague assay, the supernatants containing virus were collected and 10-fold diluted to infect Vero cells plated on 24-well plates at 90% confluence. At 2 h after infection, the supernatants were removed, the cells were washed several times with PBS, and methylcellulose (0.8%) was added. 48 h later, the cells were stained with crystal violet (0.2%) for 12 h. Plaques (PFU/ml) were then counted.

ELISA experiment

The secretion of effector cytokines from CAR-T cells was measured by ELISA kits. B7H3-CAR-T or CR2/3-B7H3-CAR-T $(10^6$



cells) were cocultured with the target tumor cells GSC-1 (10^6 cells) at ratio 1:1 in 6-wells plates. After indicated time points, the supernatants from the cocultured cells were collected and measured. The IFN γ , granzyme B, and TNF α levels in the supernatants was measured with Human IFN γ ELISA kit (EHC102g96; NeoBioscience), Human granzyme B ELISA kit (EHC117.96; NeoBioscience), and Human TNF- α ELISA kit (EHC103a96; NeoBioscience).

Ca2+ influx assay

CAR-T cells were loaded with 5 μ M Fluo-4 AM (F312; DOJINDO) and 20% pluronic F127 for 30 min at 37°C. After washing and resuspension in HBSS twice, cells were left in the dark at room temperature for 30 min. The basal line of Ca²⁺ influx was recorded for 3 min. Then VSV Δ 51 (MOI = 10) or soluble B7H3 protein (1 μ g/ml) was added into the CAR-T cells and mixed for 1 min, and the induced Ca²⁺ burst was recorded for another 12 min by flow cytometer (Cytoflex; Beckman).

Extracellular flux analysis

The mitochondrial function (oxidative phosphorylation) and glycolytic rates of CAR–T cells, which were preloaded with VSV Δ 51 for 8 h at antigen-free conditions, were assessed after washing using a Seahorse Bioanalyzer XFe96 Analyzer (Agilent Technologies). CAR–T cells were plated on Cell–Tak–coated Seahorse 96 culture plates (2 × 10⁵ cells/well). To test OCR, the addition of 1 mM oligomycin, 1 mM FCCP, 1 mM antimycin A, and rotenone were loaded according to Mito Stress test protocol. To test ECAR, 10 mM glucose, 1.5 mM oligomycin, and 50 mM 2-deoxy–D-glucose were added at the indicated times according to Seahorse XF Glycolytic Stress Test protocol.

3D tumor spheroids coculture assays

The 3D tumor spheroids were prepared by seeding GSC-1 cells (10^6 per wells) in ultralow attachment 6-well plates, cultured with DMEM/F12 media (Gibco) and added to 1% B27 (Thermo Fisher Scientific), 10 ng/ml human basic FGF, and 10 ng/ml EGF. B7H3–CAR-T or CR2/3–B7H3–CAR-T (2×10^5 per wells) were loaded with VSV Δ 51 (MOI = 10) and then were added to GSC-1 tumor spheroids. After coculture for 24 h, 3D tumor spheroids of U87 cells were stained with Calcein/PI (C2015M; Beyotime). The images were captured by a fluorescence microscope (Zeiss). The ratio of PI-positive cells was measured by flow cytometer (Beckman).

Statistical analysis

All experiments were repeated at least two times, and the data are shown as the mean \pm SD. Statistical differences between the means were compared by the two-tailed, unpaired, or paired t test for two groups, or by one-way ANOVA with Tukey's multiple comparisons test, or two-way ANOVA with Sidak's multiple comparisons test for multiple groups. For the survival curve of mice, the log-rank (Mantel-Cox) test was used for the comparison. P < 0.05 was considered statistically significant. Data were analyzed with GraphPad Prism 8.0 Software.

Study approvals

Human blood samples were anonymized in accordance with local ethical guidelines and the Declaration of Helsinki and was approved by the Clinical Ethics Review Board of the Guangdong Provincial People's Hospital (approval number KY-N-2021-070). All mouse experiments strictly followed the ethical regulations and were approved by the Ethics Review Committee of Guangdong Provincial People's Hospital (approval number KY-N-2022-129).

Online supplemental material

Fig. S1 shows that the insertion of CR2/3 domain slightly reduced the tumor-killing capacity of CAR-T cells, while significantly improved the viral delivery of VSVΔ51 to tumor cells. Fig. S2 shows that the incubation of soluble CAR antigen did not increase the functional activity and tumor-killing capacity of B7H3–CAR-T cells. Fig. S3 shows the *in vitro* restimulation assay for measuring the persistence of CAR-T cells under chronic tumor exposure. Fig. S4 shows the comparison of different CAR-T/OV combination strategies. Fig. S5 shows the safety and potential toxicity evaluation of the CR2/3–CAR-T^{VSV} treatment.

Data availability

The transcriptomic data that support the findings of this study are openly available in GEO (accession numbers GSE273425 and GSE302980). Materials generated in the course of this work may be obtained through a material transfer agreement.

Acknowledgments

We thank Prof. Guangmei Yan (Zhongshan School of Medicine, Sun Yat-sen University) and Prof. Deyin Guo (Guangzhou National Laboratory, Guangzhou) for their advice.

This work was supported by grants from the National Natural Science Foundation of China (NSFC) (grant no. 82173829 to F. Xing), Guangdong Special Support Program for Young Top Talents (2023TQ07Y333 to F. Xing), Youth Talent Development Grand of Southern Medical University (G623281132 to F. Xing), the Important Key Program of NSFC (92169201, 92369205 to H. Zhang), and the Key R&D Program of the Department of Science and Technology of Guangdong (2022B1111020004 to H. Zhang).

Author contributions: F. Xing: conceptualization, data curation, formal analysis, funding acquisition, investigation, methodology, project administration, validation, visualization, and writing—original draft, review, and editing. X. Wang: data curation and investigation. Z. Li: data curation and investigation. L. Zheng: data curation and investigation. Z. Huang: data curation and investigation. J. Guo: methodology and software. Z. Xi: investigation. H. Feng: investigation. B. Xia: investigation. Y. Lin: investigation. F. Yu: data curation and investigation. J. Chen: conceptualization, data curation, formal analysis, and supervision. H. Zhang: conceptualization, funding acquisition, supervision, validation, and writing—review and editing.

Disclosures: F. Xing and H. Zhang reported a patent to CN202510447007.6 pending. No other disclosures were reported.



Submitted: 8 October 2024 Revised: 6 February 2025 Accepted: 29 July 2025

References

- Ajina, A., and J. Maher. 2017. Prospects for combined use of oncolytic viruses and CAR T-cells. J. Immunother. Cancer. 5:90. https://doi.org/10.1186/ s40425-017-0294-6
- Albelda, S.M. 2024. CAR T cell therapy for patients with solid tumours: Key lessons to learn and unlearn. Nat. Rev. Clin. Oncol. 21:47-66. https://doi.org/10.1038/s41571-023-00832-4
- Brown, C.E., B. Badie, M.E. Barish, L. Weng, J.R. Ostberg, W.-C. Chang, A. Naranjo, R. Starr, J. Wagner, C. Wright, et al. 2015. Bioactivity and safety of IL13Rα2-redirected chimeric antigen receptor CD8+T cells in patients with recurrent glioblastoma. *Clin. Cancer Res.* 21:4062–4072. https://doi.org/10.1158/1078-0432.CCR-15-0428
- Chen, X., J. Liu, Y. Li, Y. Zeng, F. Wang, Z. Cheng, H. Duan, G. Pan, S. Yang, Y. Chen, et al. 2023. IDH1 mutation impairs antiviral response and potentiates oncolytic virotherapy in glioma. *Nat. Commun.* 14:6781. https://doi.org/10.1038/s41467-023-42545-3
- Chen, Y., X. Chen, W. Bao, G. Liu, W. Wei, and Y. Ping. 2024. An oncolytic virus-T cell chimera for cancer immunotherapy. *Nat. Biotechnol.* 42: 1876–1887. https://doi.org/10.1038/s41587-023-02118-7
- Chockley, P.J., J. Ibanez-Vega, G. Krenciute, L.J. Talbot, and S. Gottschalk. 2023. Synapse-tuned CARs enhance immune cell anti-tumor activity. *Nat. Biotechnol.* 41:1434-1445. https://doi.org/10.1038/s41587-022
- Davenport, A.J., R.S. Cross, K.A. Watson, Y. Liao, W. Shi, H.M. Prince, P.A. Beavis, J.A. Trapani, M.H. Kershaw, D.S. Ritchie, et al. 2018. Chimeric antigen receptor T cells form nonclassical and potent immune synapses driving rapid cytotoxicity. Proc. Natl. Acad. Sci. USA. 115:E2068–E2076. https://doi.org/10.1073/pnas.1716266115
- Dewdney, B., M.R. Jenkins, S.A. Best, S. Freytag, K. Prasad, J. Holst, R. Endersby, and T.G. Johns. 2023. From signalling pathways to targeted therapies: Unravelling glioblastoma's secrets and harnessing two decades of progress. Signal Transduct. Target. Ther. 8:400. https://doi.org/10.1038/s41392-023-01637-8
- Du, H., K. Hirabayashi, S. Ahn, N.P. Kren, S.A. Montgomery, X. Wang, K. Tiruthani, B. Mirlekar, D. Michaud, K. Greene, et al. 2019. Antitumor responses in the absence of toxicity in solid tumors by targeting B7-H3 via chimeric antigen receptor T cells. Cancer Cell. 35:221–237.e8. https://doi.org/10.1016/j.ccell.2019.01.002
- Evgin, L., A.L. Huff, P. Wongthida, J. Thompson, T. Kottke, J. Tonne, M. Schuelke, K. Ayasoufi, C.B. Driscoll, K.G. Shim, et al. 2020. Oncolytic virus-derived type I interferon restricts CAR T cell therapy. Nat. Commun. 11:3187. https://doi.org/10.1038/s41467-020-17011-z
- Evgin, L., T. Kottke, J. Tonne, J. Thompson, A.L. Huff, J. van Vloten, M. Moore, J. Michael, C. Driscoll, J. Pulido, et al. 2022. Oncolytic virus-mediated expansion of dual-specific CAR T cells improves efficacy against solid tumors in mice. Sci. Transl. Med. 14:eabn2231. https://doi.org/10.1126/scitranslmed.abn2231
- Fauci, J.M., F. Sabbatino, Y. Wang, A.I. Londoño-Joshi, J.M. Straughn Jr., C.N. Landen, S. Ferrone, and D.J. Buchsbaum. 2014. Monoclonal antibody-based immunotherapy of ovarian cancer: Targeting ovarian cancer cells with the B7-H3-specific mAb 376.96. Gynecol. Oncol. 132:203–210. https://doi.org/10.1016/j.ygyno.2013.10.038
- Finkelshtein, D., A. Werman, D. Novick, S. Barak, and M. Rubinstein. 2013. LDL receptor and its family members serve as the cellular receptors for vesicular stomatitis virus. *Proc. Natl. Acad. Sci. USA.* 110:7306–7311. https://doi.org/10.1073/pnas.1214441110
- Hammer, J.A., J.C. Wang, M. Saeed, and A.T. Pedrosa. 2019. Origin, organization, dynamics, and function of actin and actomyosin networks at the T cell immunological synapse. Annu. Rev. Immunol. 37:201–224. https://doi.org/10.1146/annurev-immunol-042718-041341
- Jackson, C.M., J. Choi, and M. Lim. 2019. Mechanisms of immunotherapy resistance: Lessons from glioblastoma. Nat. Immunol. 20:1100–1109. https://doi.org/10.1038/s41590-019-0433-y
- Khong, H.T., and N.P. Restifo. 2002. Natural selection of tumor variants in the generation of "tumor escape" phenotypes. Nat. Immunol. 3:999–1005. https://doi.org/10.1038/nii102-999
- Li, Y., M. Huang, M. Wang, Y. Wang, P. Deng, C. Li, J. Huang, H. Chen, Z. Wei, Q. Ouyang, et al. 2024. Tumor cells impair immunological synapse

- formation via central nervous system-enriched metabolite. *Cancer Cell.* 42:985–1002.e18. https://doi.org/10.1016/j.ccell.2024.05.006
- Liu, D., Y.T. Bryceson, T. Meckel, G. Vasiliver-Shamis, M.L. Dustin, and E.O. Long. 2009. Integrin-dependent organization and bidirectional vesicular traffic at cytotoxic immune synapses. *Immunity*. 31:99–109. https://doi.org/10.1016/j.immuni.2009.05.009
- Menk, A.V., N.E. Scharping, R.S. Moreci, X. Zeng, C. Guy, S. Salvatore, H. Bae, J. Xie, H.A. Young, S.G. Wendell, and G.M. Delgoffe. 2018. Early TCR signaling induces rapid aerobic glycolysis enabling distinct acute T cell effector functions. Cell Rep. 22:1509–1521. https://doi.org/10.1016/j.celrep.2018.01.040
- Nie, J., Q. Li, J. Wu, C. Zhao, H. Hao, H. Liu, L. Zhang, L. Nie, H. Qin, M. Wang, et al. 2020. Quantification of SARS-CoV-2 neutralizing antibody by a pseudotyped virus-based assay. *Nat. Protoc.* 15:3699–3715. https://doi.org/10.1038/s41596-020-0394-5
- Nikolic, J., L. Belot, H. Raux, P. Legrand, Y. Gaudin, and A.A. Albertini. 2018. Structural basis for the recognition of LDL-receptor family members by VSV glycoprotein. Nat. Commun. 9:1029. https://doi.org/10.1038/s41467 -018-03432-4
- Nishio, N., I. Diaconu, H. Liu, V. Cerullo, I. Caruana, V. Hoyos, L. Bouchier-Hayes, B. Savoldo, and G. Dotti. 2014. Armed oncolytic virus enhances immune functions of chimeric antigen receptor-modified T cells in solid tumors. Cancer Res. 74:5195–5205. https://doi.org/10.1158/0008-5472_.CAN-14-0697
- Orange, J.S. 2008. Formation and function of the lytic NK-cell immunological synapse. *Nat. Rev. Immunol.* 8:713–725. https://doi.org/10.1038/nri2381
- Park, A.K., Y. Fong, S.-I. Kim, J. Yang, J.P. Murad, J. Lu, B. Jeang, W.-C. Chang, N.G. Chen, S.H. Thomas, et al. 2020. Effective combination immunotherapy using oncolytic viruses to deliver CAR targets to solid tumors. Sci. Transl. Med. 12:eaaz1863. https://doi.org/10.1126/scitranslmed.aaz1863
- Qiao, Y., J. Chen, X. Wang, S. Yan, J. Tan, B. Xia, Y. Chen, K. Lin, F. Zou, B. Liu, et al. 2023. Enhancement of CAR-T cell activity against cholangiocarcinoma by simultaneous knockdown of six inhibitory membrane proteins. Cancer Commun. 43:788–807. https://doi.org/10.1002/cac2.12452
- Rosewell Shaw, A., C.E. Porter, N. Watanabe, K. Tanoue, A. Sikora, S. Gott-schalk, M.K. Brenner, and M. Suzuki. 2017. Adenovirotherapy delivering cytokine and checkpoint inhibitor augments CAR T cells against metastatic head and neck cancer. *Mol. Ther.* 25:2440–2451. https://doi.org/10.1016/j.ymthe.2017.09.010
- Schaff, L.R., and I.K. Mellinghoff. 2023. Glioblastoma and other primary brain malignancies in adults: A review. *Jama*. 329:574–587. https://doi.org/10.1001/jama.2023.0023
- Smith-Garvin, J.E., G.A. Koretzky, and M.S. Jordan. 2009. T cell activation.

 Annu. Rev. Immunol. 27:591-619. https://doi.org/10.1146/annurev.immunol.021908.132706
- Stojdl, D.F., B.D. Lichty, B.R. tenOever, J.M. Paterson, A.T. Power, S. Knowles, R. Marius, J. Reynard, L. Poliquin, H. Atkins, et al. 2003. VSV strains with defects in their ability to shutdown innate immunity are potent systemic anti-cancer agents. *Cancer Cell*. 4:263–275. https://doi.org/10 .1016/s1535-6108(03)00241-1
- Sun, C., P. Shou, H. Du, K. Hirabayashi, Y. Chen, L.E. Herring, S. Ahn, Y. Xu, K. Suzuki, G. Li, et al. 2020. THEMIS-SHP1 recruitment by 4-1BB tunes LCK-mediated priming of chimeric antigen receptor-redirected T cells. Cancer Cell. 37:216–225.e6. https://doi.org/10.1016/j.ccell.2019.12.014
- Tanoue, K., A. Rosewell Shaw, N. Watanabe, C. Porter, B. Rana, S. Gottschalk, M. Brenner, and M. Suzuki. 2017. Armed oncolytic adenovirus-expressing PD-L1 mini-body enhances antitumor effects of chimeric antigen receptor T cells in solid tumors. *Cancer Res.* 77:2040–2051. https://doi.org/10.1158/0008-5472.CAN-16-1577
- van den Bent, M.J., M. Geurts, P.J. French, M. Smits, D. Capper, J.E.C. Bromberg, and S.M. Chang. 2023. Primary brain tumours in adults. *Lancet*. 402:1564-1579. https://doi.org/10.1016/S0140-6736(23)01054-1
- Wang, G., Z. Zhang, K. Zhong, Z. Wang, N. Yang, X. Tang, H. Li, Q. Lu, Z. Wu, B. Yuan, et al. 2023. CXCL11-armed oncolytic adenoviruses enhance CAR-T cell therapeutic efficacy and reprogram tumor microenvironment in glioblastoma. Mol. Ther. 31:134–153. https://doi.org/10.1016/j.ymthe.2022.08.021
- Wang, X., X. Wu, B. Tan, L. Zhu, Y. Zhang, L. Lin, Y. Xiao, A. Sun, X. Wan, S. Liu, et al. 2024. Allogeneic CD19-targeted CAR-T therapy in patients with severe myositis and systemic sclerosis. Cell. 187:4890–4904.e9. https://doi.org/10.1016/j.cell.2024.06.027
- Watanabe, K., Y. Luo, T. Da, S. Guedan, M. Ruella, J. Scholler, B. Keith, R.M. Young, B. Engels, S. Sorsa, et al. 2018. Pancreatic cancer therapy with combined mesothelin-redirected chimeric antigen receptor T cells and



- cytokine-armed oncolytic adenoviruses. *JCI Insight*. 3:e99573. https://doi.org/10.1172/jci.insight.99573
- Xiao, J., J. Liang, J. Fan, P. Hou, X. Li, H. Zhang, K. Li, L. Bu, P. Li, M. He, et al. 2022. CDK4/6 inhibition enhances oncolytic virus efficacy by potentiating tumor-selective cell killing and T-cell activation in refractory glioblastoma. Cancer Res. 82:3359–3374. https://doi.org/10.1158/0008 -5472.CAN-21-3656
- Xing, F., Y. Luan, J. Cai, S. Wu, J. Mai, J. Gu, H. Zhang, K. Li, Y. Lin, X. Xiao, et al. 2017. The anti-warburg effect elicited by the cAMP-PGC1α pathway drives differentiation of glioblastoma cells into astrocytes. Cell Rep. 18:468–481. https://doi.org/10.1016/j.celrep.2016.12.037
- Xing, F., J. Xiao, J. Wu, J. Liang, X. Lu, L. Guo, P. Li, P. Hou, C. Li, and D. Guo. 2021. Modulating the tumor microenvironment via oncolytic virus and
- PI3K inhibition synergistically restores immune checkpoint therapy response in PTEN-deficient glioblastoma. *Signal Transduct. Target. Ther.* 6:275. https://doi.org/10.1038/s41392-021-00609-0
- Xu, X., H. Chen, Z. Ren, X. Xu, W. Wu, H. Yang, J. Wang, Y. Zhang, Q. Zhou, H. Li, et al. 2024. Phase separation of chimeric antigen receptor promotes immunological synapse maturation and persistent cytotoxicity. *Immunity*. 57:2755-2771.e8. https://doi.org/10.1016/j.immuni.2024.11.005
- Zheng, N., J. Fang, G. Xue, Z. Wang, X. Li, M. Zhou, G. Jin, M.M. Rahman, G. McFadden, and Y. Lu. 2022. Induction of tumor cell autosis by myxoma virus-infected CAR-T and TCR-T cells to overcome primary and acquired resistance. Cancer Cell. 40:973–985.e7. https://doi.org/10.1016/j.ccell.2022.08.001



Supplemental material

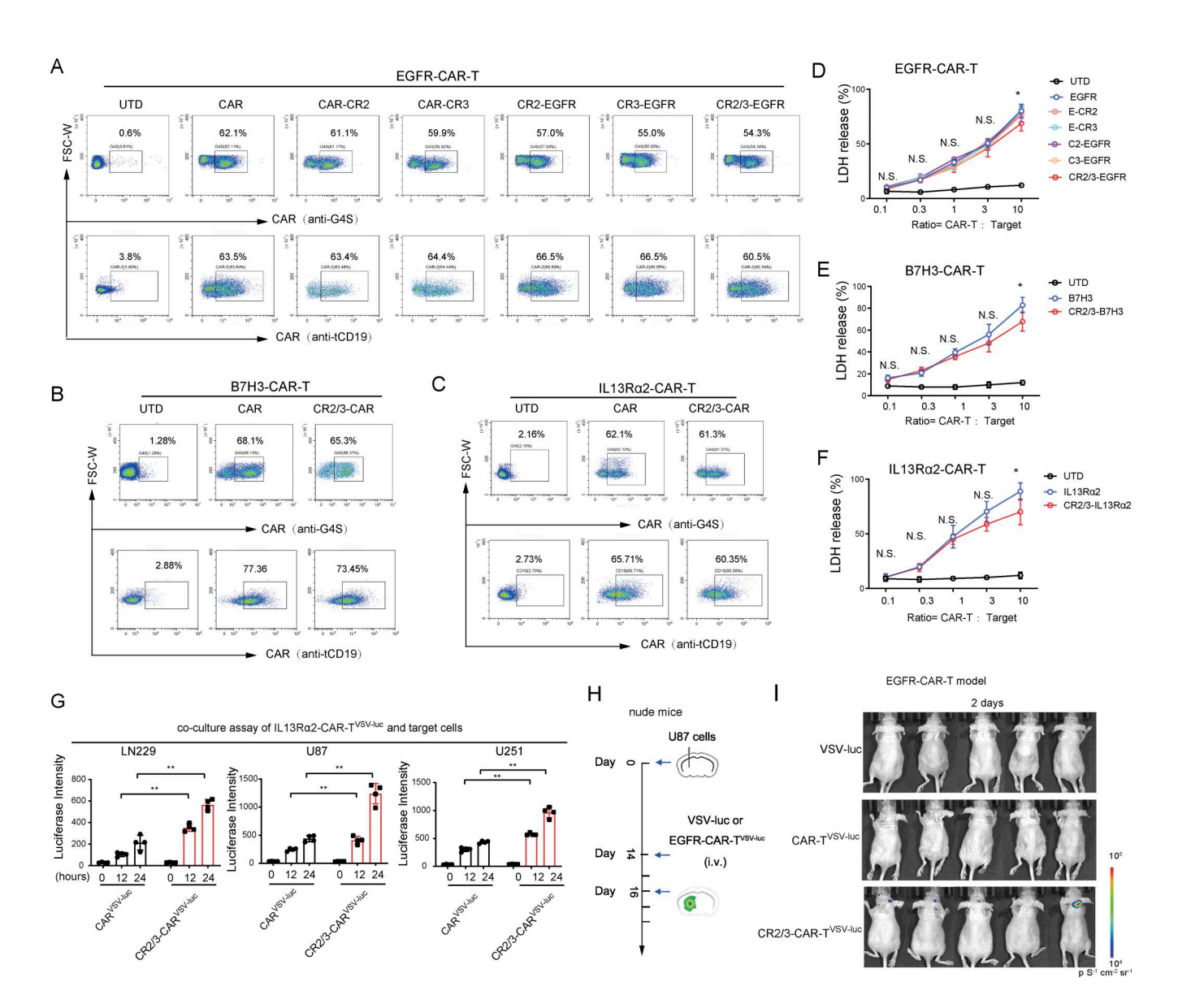


Figure S1. Insertion of CR2/3 domain slightly reduced the tumor-killing capacity of CAR-T cells, while significantly improved the viral delivery of VSVΔ51 to tumor cells. (A–C) CAR expression efficiency of EGFR–CAR-T model (A), B7H3–CAR-T (B), and IL13Rα2–CAR-T (C). The transfection efficiency of CAR was evaluated by detecting the expression of the G4S linker and reporter gene truncated CD19 in CAR-T cells. A representative experiment is shown, repeated at least twice with similar results. (D–F) Cell cytotoxicity was measured by LDH release assay of EGFR–CAR-T model (D), B7H3–CAR-T (E), and IL13Rα2–CAR-T (F). U87 cells were cocultured with CAR-T cells at different ratios for 24 h, and then the LDH release from U87 cells was measured. The cell cytotoxicity experiments were performed independently three times (n = 3 biological replicates). (G) Luciferase activity was measured in coculture glioma cells with IL13Rα2–CAR-T preloaded with the VSV-luc (n = 4 biological replicates). (H and I) In vivo evaluation for viral delivery of EGFR–CAR-T model. (H) Diagram depicting the monitoring of the *in vivo* virus distribution via bioluminescence imaging of luciferase in U87 xenograft mice. (I) Monitoring of the *in vivo* virus distribution via bioluminescence imaging of luciferase in U87 xenograft mice. (I) Monitoring of the *in vivo* virus distribution via bioluminescence imaging of luciferase in U87 xenograft mice. (I) Monitoring of the *in vivo* virus distribution via bioluminescence imaging of luciferase in U87 xenograft mice. (I) Monitoring of the *in vivo* virus distribution via bioluminescence imaging of luciferase in U87 xenograft mice. (I) Monitoring of the *in vivo* virus distribution via bioluminescence imaging of luciferase in U87 xenograft mice. (I) Monitoring of the *in vivo* virus distribution via bioluminescence imaging of luciferase in U87 xenograft mice. (I) Monitoring of the *in vivo* virus distribution via bioluminescence imaging of luciferase in U87 xenograft mice. (I) Monitoring of the *in vivo* vir



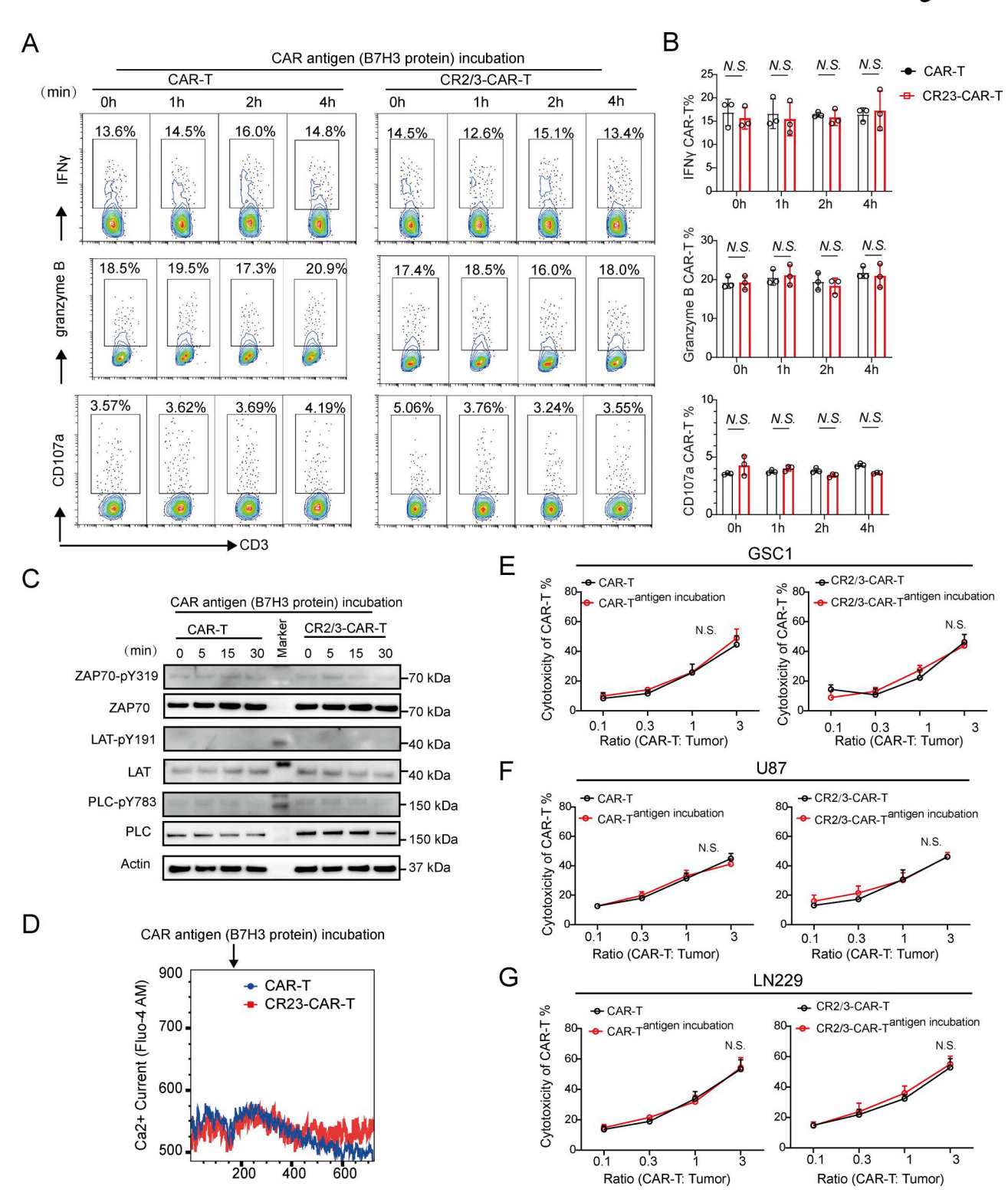


Figure S2. The incubation of soluble CAR antigen did not increase the functional activity and tumor-killing capacity of B7H3-CAR-T cells. (A and B) Flow cytometry analysis for functional activity of CAR-T cells incubated with tumor antigen B7H3 protein (0.5 μ g/ml) for indicated time from 1 to 4 h. The functional activity of CAR-T cells was measured by the expression of IFN γ , CD107a, and granzyme B (n = 3 biological replicates). (C) Immunoblotting analysis for CAR-mediated proximal signaling. The phosphorylation of ZAP70, LAT, and PLC γ of CAR-T were measured after exposure to B7H3 protein (0.5 μ g/ml) at indicated times from 0 to 30 min. A representative experiment is shown, repeated twice. (D) Ca²⁺ influx was measured by Fluo-4 fluorescence probe in CAR-T cells. CAR-T cells were incubated with soluble B7H3 protein (0.5 μ g/ml), and then the MFI of Fluo-4 was measured by flow cytometry in real time. A representative experiment is shown, repeated twice. (E–G) Cytotoxic activities of CAR-T cells against GSC-1 (E), U87 (F), and LN229 (G) cells (n = 3 biological replicates). CAR-T cells preincubated with 0.5 μ g/ml soluble B7H3 protein for 1 h, and then U87-B7H3-KO cells were cocultured with preincubated CAR-T cells at the indicated ratio from 0.1:1 to 3:1 (CAR-T:Tumor) for 24 h. Data represent the mean \pm SD from three independent experiments. Statistics by unpaired two-tailed Student's t test (B) or two-way ANOVA (E–G). *, P < 0.05; **, P < 0.01; N.S., no significance. Source data are available for this figure: SourceData FS2.



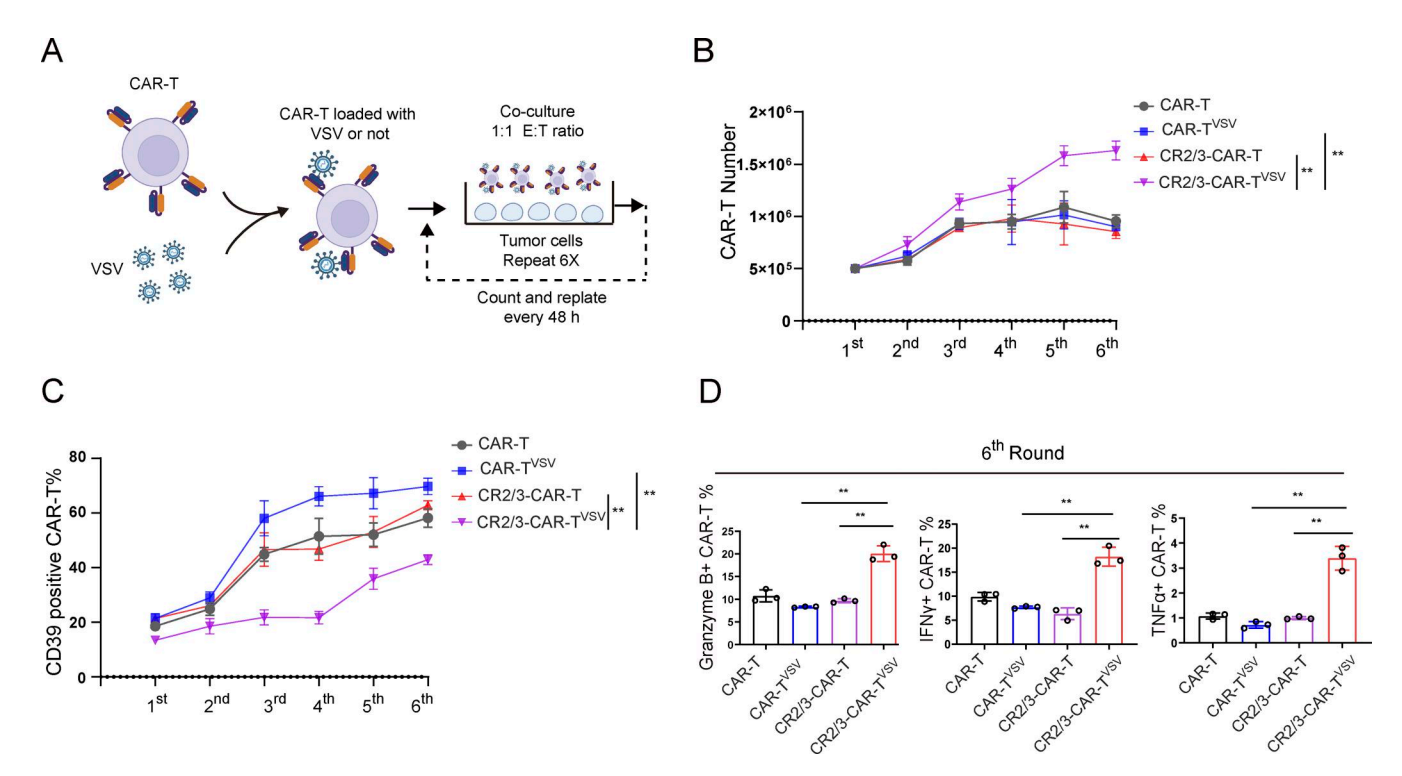


Figure S3. The *in vitro* restimulation assay for measuring the persistence of CAR-T cells under chronic tumor exposure. (A) Schematic of experiment for modeling T cell persistence *in vitro*. (B) CAR-T cell expansion curve upon chronic tumor exposure. CAR-T cells (5×10^5) were mixed with U87 cells (5×10^5) in 24 wells. After eradication of tumor cells in 2 days, CAR-T cell numbers were counted and were added to fresh tumor cells for another round of tumor challenge (n = 3 biological replicates). (C) The exhaustion marker CD39 levels were measured by flow cytometry after each stimulation (n = 3 biological replicates). (D) The functional markers of CAR-T cells were measured after the sixth round of tumor challenge (n = 3 biological replicates). Data represent the mean \pm SD from three independent experiments. Statistics by two-way ANOVA (B and C) or one-way ANOVA with Tukey's multiple comparison test (D). *, P < 0.05; **, P < 0.01; N.S., no significance.



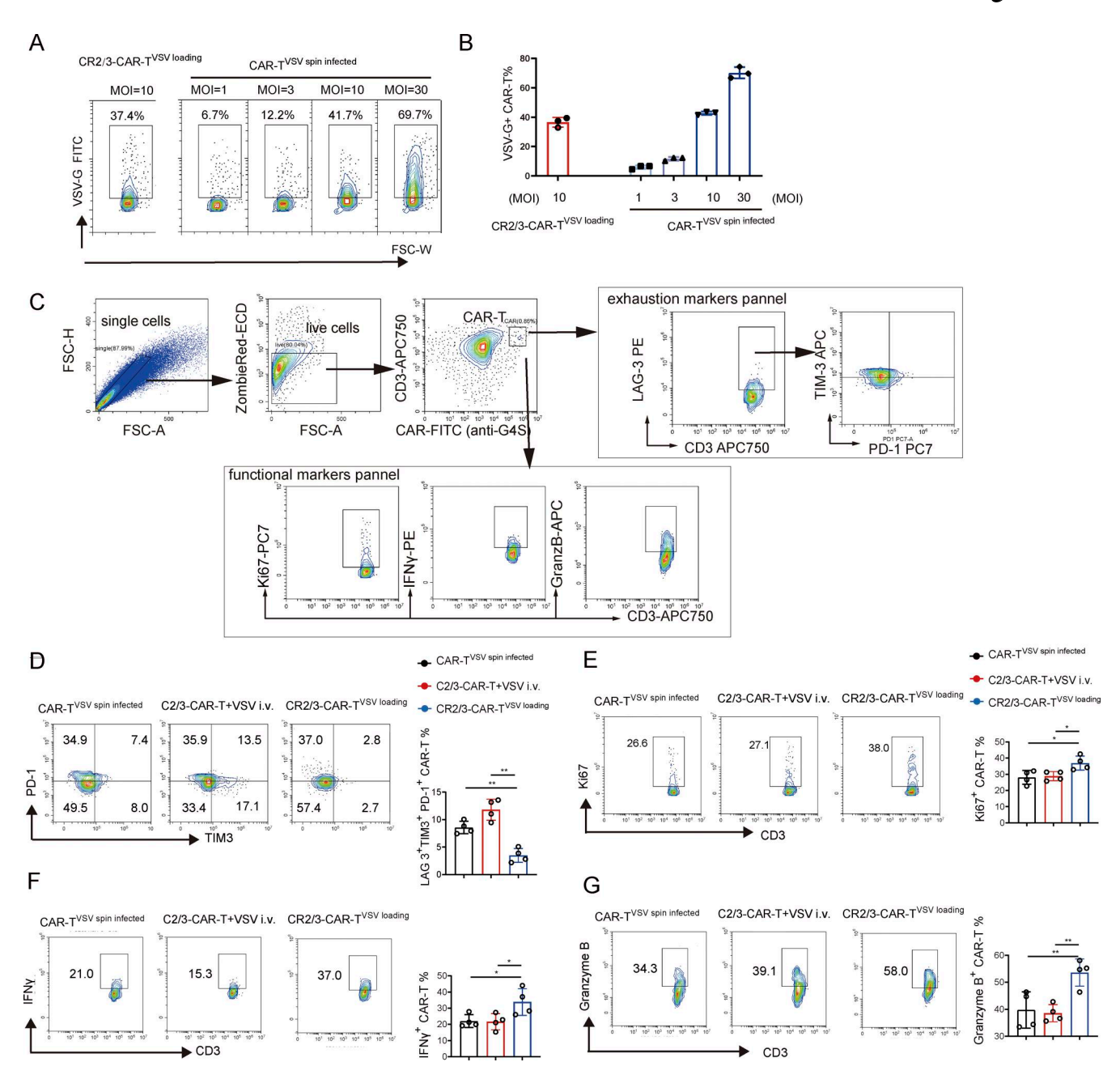


Figure S4. The comparison of different CAR-T/OV combination strategies. (A and B) Comparison of the viral loading amount between CAR-T^{VSV} spin-infected and CR2/3–CAR-T^{VSV} loading. (A) Flow cytometry analysis for viral loading efficiency by measuring the surface VSV-G expression on CAR-T cells. The representative flow cytometry plots are shown. (B) The ratio of VSV-G–positive CAR-T cells was quantified. For CAR-T^{VSV} spin-infected group, B7H3–CAR-T cells adopted a virus transduction protocol (centrifugation 2,000 g for 2 h) to promote the infection of VSV on CAR-T cells at a MOI of 1, 3, 10, and 30. For CR2/3–CAR-T^{VSV} loading group, CR2/3–B7H3–CAR-T cells were specifically loaded with VSV Δ 51 (MOI = 10) in 4°C for 1 h. Then the viral loading was evaluated by surface VSV-G expression on CAR-T cells (n = 3 biological replicates). (C) Depiction of the gating strategy of flow cytometry for analyzing intra-tumoral CAR-T cells. The representative flow cytometry plots are shown for gating the exhaustion markers, including LAG-3, PD-1, and TIM-3, or gating the functional markers, including granzyme B, TNF α , and IFNY. (D–G) Flow cytometry for analyzing the T exhaustion and functional activity of intra-tumoral CAR-T cells. Flow cytometry analysis of for analyzing the T exhaustion and functional activity of intra-tumoral CAR-T cells in Fig. 6 H. The ratio of PD-1 TIM-3* LAG+CAR-T (D), Ki67 expression (E), IFNY expression (F), and granzyme B expression (G) of intra-tumoral CAR-T cells were analyzed. Left panel: Representative flow cytometry plots. Right panel: The quantitative analysis of the ratio of PD-1 and TIM3-positive CAR-T (n = 4 biological replicates). Data represent the mean \pm SD from three independent experiments (B) or one representative from two independent experiments (D–G). Statistics by one-way ANOVA with Tukey's multiple comparison test (D–G). *, P < 0.05; ***, P < 0.01; N.S., no significance.



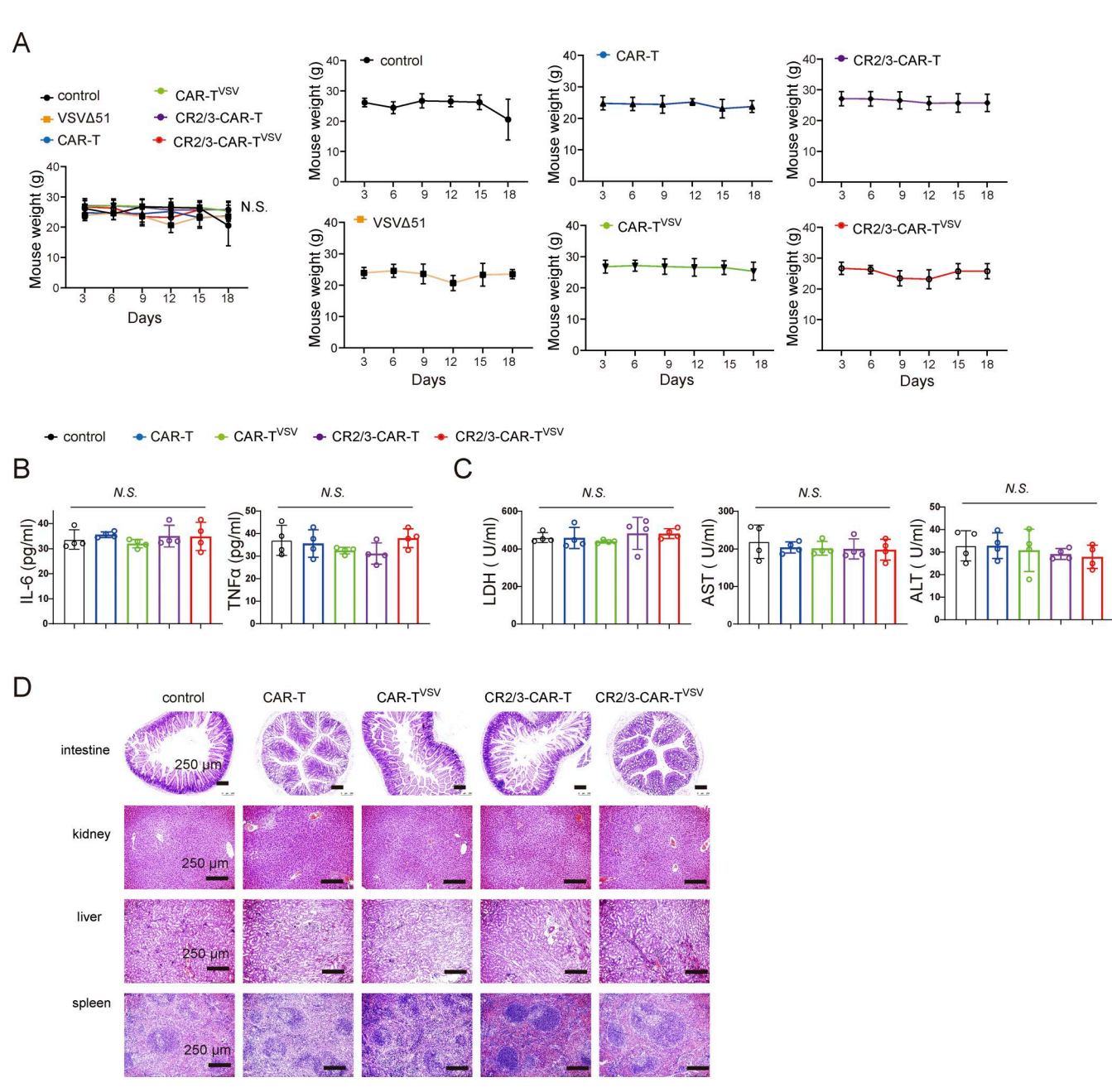


Figure S5. **Safety and potential toxicity evaluation of the CR2/3-CAR-T^{VSV} treatment. (A)** Body weight of NCG mice bearing U87 intracranial xenografts were measured every 3 days (n = 4 mice). **(B)** The inflammatory cytokine (TNF α and IL-6) levels in the serum of mice 9 days after the indicated treatments (n = 4 mice). **(C)** In vivo biosafety analysis of LDH, aspartate aminotransferase (AST), and alanine transaminase (ALT) in the mice 9 days after the indicated treatment. **(D)** H&E staining of vital tissues, including kidney, intestine, liver, and spleen. A representative experiment is shown, repeated once. Data represent the mean \pm SD from one representative from two independent experiments (A and B). Statistics by two-way ANOVA (A) and one-way ANOVA (B and C). *, P < 0.05; **, P < 0.01; N.S., no significance.